



## A two-phase theoretical model incorporating liquid film dynamics for pulsating heat pipes

Ying Liu<sup>a</sup>, Yuhao Yan<sup>a</sup>, Xilei Wu<sup>a</sup>, Kangli Bao<sup>a</sup>, Jiali Yang<sup>a</sup>, Maojin Zeng<sup>b</sup>, Xiaohong Han<sup>a,\*</sup>

<sup>a</sup> Zhejiang Key Laboratory of Refrigeration and Cryogenic Technology, Institute of Refrigeration and Cryogenics, Zhejiang University, Hangzhou 310027, PR China

<sup>b</sup> School of Energy and Power Engineering, Xi'an Jiaotong University, Xi'an 710049, PR China

### ARTICLE INFO

#### Keywords:

Two-phase numerical model  
Pulsating heat pipe  
Liquid film dynamics  
Heat transfer distance

### ABSTRACT

Pulsating Heat Pipes (PHPs) hold significant potential for efficient thermal management of electronic devices due to their superior heat transfer capabilities, flexible design, and cost-effective manufacturing. However, in view of the fact that there may be different heat transfer distances between heat sources and heat sinks, the widespread application of PHPs has been limited by the lack of accurate models and experimental data to predict and understand their flow and heat transfer performance at varying heat transfer distances. To address these limitations, a two-phase heat and mass transfer model incorporating liquid film dynamics was developed and partial visualization experiments were conducted to validate the reliability of the theoretical model. Based on these, the flow and heat transfer performance of R1336mzz(Z)-PHPs under various heat transfer distances were numerically simulated and experimentally investigated. The flow and heat transfer characteristics of R1336mzz(Z)-PHPs were compared with those of water-PHPs and ethanol-PHPs to investigate the influence of working fluids on the operating performance of PHPs through numerical simulation. The results revealed that the two-phase heat and mass transfer model could capture the local dry-out phenomenon and accurately simulate the heat and mass transfer process in PHPs through the comparison of experimental results with simulation results. According to simulation results, increasing heat input enhanced both flow and heat transfer performance for R1336mzz(Z)-PHPs, especially at shorter heat transfer distances. There was an optimal heat transfer distance at which the flow and heat transfer performance of the PHP were best. Compared to water and ethanol, R1336mzz(Z) generated a greater driving force while experiencing lower flow resistance, resulting in a higher average flow velocity of the working fluid. This enabled the transition from oscillatory flow to one-way circulation flow at various heat transfer distances and avoided the occurrence of local dry-out, leading to superior flow performance. Besides, the performance of the R1336mzz(Z)-PHP was relatively less affected by heat transfer distance. Even at a large heat transfer distance, R1336mzz(Z) maintained superior flow and heat transfer performance.

### 1. Introduction

With the rapid development of electronic devices, especially the popularity of high-performance computing equipment and miniaturized devices, heat dissipation has become a key factor affecting the stability, performance and life of electronic devices [1]. While advanced cooling technologies like immersion, microchannel, and spray cooling offer significant benefits, they often come with increased complexity and cost [2]. Heat pipes, as passive cooling technologies, provide a versatile and efficient alternative due to their simplicity, compact design, and zero

additional energy consumption. This makes them well-suited for a variety of applications, including electronics cooling, aerospace, renewable energy systems, and industrial processes.

Among the various types of heat pipes, pulsating heat pipes (PHPs) show unique operating mechanisms and application advantages due to their capillary-wick-free structure. The structure of a PHP is straightforward, comprising a slender tube shaped into multiple U-shaped loops. The tube is partially filled with two-phase working fluid. During operation, the hot end (evaporation section) absorbs heat, causing the liquid to evaporate into bubbles. As the bubbles expand, the high pressure in the evaporation section pushes the working fluid toward the cold end

\* Corresponding author: Zhejiang University Key Laboratory of Refrigeration and Cryogenic Technology, No 38,Zheda Road, Hangzhou, Hangzhou, Zhejiang 310027, PR China.

E-mail address: hanxh66@zju.edu.cn (X. Han).

<b>Nomenclature</b>		<b>Subscripts</b>
<i>T</i>	Temperature (°C)	c Condensation section
<i>q</i>	Heat flux (W/m <sup>2</sup> )	s Static
<i>h<sub>fg</sub></i>	Latent heat of vaporization (J/kg)	v Vapor
<i>We</i>	Weber number	ac Advancing contact angle
<i>K</i>	Local resistance coefficient at turns	i Number of the liquid slugs and vapor plugs
<i>Ca</i>	Capillary number	sim Simulation
<i>A</i>	Area(m <sup>2</sup> )	w Wall
<i>f</i>	Friction factor	nb Nucleate boiling
<i>m</i>	Mass (kg)	wf From wall to fluid
<i>F</i>	Force (N)	f Fluid
<i>θ</i>	Contact angle	left Left unit
<i>p</i>	pressure (Pa)	f <sub>0</sub> Initial liquid film
<i>N</i>	Number of turns	e Evaporation section
<i>R</i>	Thermal resistant (°C/W)	in Internal
<i>d</i>	Diameter (m)	l Liquid
<i>g</i>	Gravity acceleration (m/s <sup>2</sup> )	sat Saturation
<i>h</i>	Heat transfer coefficient (W/(m <sup>2</sup> • °C))	rc Receding contact angle
<i>Re</i>	Reynolds number	exp Experiment
<i>Pr</i>	Prandtl number	crit Critical
<i>̄T</i>	Average temperature (°C)	sg Single phase
<i>x</i>	Coordinate value	p Driving force
<i>S</i>	Nucleate boiling suppression factor	new New unit
<i>R</i>	Universal gas constant	right Right unit
<i>u</i>	Velocity (m/s)	a Adiabatic section
<i>β</i>	The angle between the direction of flow and the direction of gravity	j Number of the wall unit
<i>Q</i>	Heat input (W)	cr Cross-section
<i>L</i>	Length (m)	
<i>c<sub>p</sub></i>	Specific heat capacity (J/kg·°C)	
<i>Abbreviation</i>		<i>Greek symbols</i>
PHP	Pulsating heat pipe	λ Thermal conductivity(W/m·°C)
FR	Filling ratio	ρ Density (kg/m <sup>3</sup> )
		σ Surface tension (N/m)
		δ Liquid film thickness (m)
		μ Dynamic viscosity (Pa·s)

(condensation section). At the cold end, the bubbles condense with heat releasing. The amount of liquid in the cold end gradually increases and the liquid flows back to the hot end. Heat transfer in the PHP is driven by the natural pulsation of the working fluid. This self-excited oscillatory heat transfer mechanism gives PHPs a simpler design, broader operating range, and highly efficient heat transfer capacity. As a result, pulsating heat pipes hold significant potential for application in complex assembly environments.

The operating environment (e.g., inclination angle, filling ratio, etc.), working fluid's thermal properties, and design parameters (e.g., number of turns, channel diameter, etc.) all affect the operating performance of PHPs [3]. Besides, different heat transfer distances may exist between heat sources and heat sinks in the cooling system of data centers. Therefore, the heat transfer distance is also an important parameter to be considered for heat dissipation design. However, there are still many problems that hinder the application of PHPs at different heat transfer distances.

For the theoretical research, Wang et al. [4] and Nikolayev et al. [5] have provided comprehensive reviews on the theoretical studies about thermo-hydrodynamic characteristics of PHPs. Recent reviews indicate that researchers have explored various approaches to model PHPs, including Artificial Neural Networks (ANN) [6], one-dimensional self-programming modeling [7] and Computational Fluid Dynamics (CFD) [8]. The ANN method is promising in predicting the performance of PHPs. ANN models are typically trained on data and can provide accurate predictions, which can be advantageous in certain situations when computational resources or time are limited. However, ANN models are

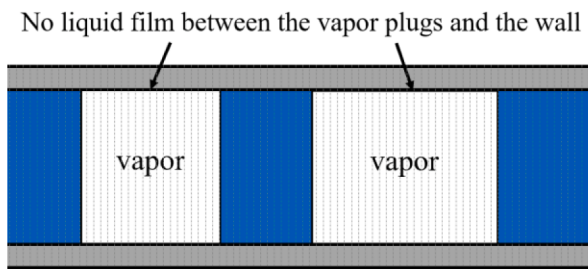
essentially black-box analyses and lack detailed physical explanations of fluid and heat transfer phenomena [6]. In contrast, CFD methods can achieve highly detailed modeling but are constrained by significant computational costs and long processing times. As a result, one-dimensional self-programming numerical simulations, which involve establishing and solving the governing equations for mass, momentum, and energy, have emerged as an ideal and cost-effective candidate for investigating the fundamental physical principles and optimizing the design of PHPs [9].

When modeling PHPs, the accurate calculation of liquid film dynamics can't be ignored. Because the evaporation of liquid film is one of the primary heat transfer mechanisms of PHPs [10] and plays a crucial role in the self-excited oscillation of the working fluid in the PHP [11]. The most intense heat and mass exchange takes place across the thin liquid film [12]. Therefore, it is crucial to accurately model the heat and mass transfer process in the liquid film. Table 1 summarizes the development in previous self-programming numerical models of PHPs and Fig. 1 demonstrates the differences between these models in modeling liquid film dynamics. Based on the differences in modeling the liquid film dynamics, self-programming numerical models of PHPs can be divided into four generations. In the first-generation models, liquid film was not considered. These models provided initial insights into the operation mechanism of PHPs [13]. In the second-generation models, each vapor plug was always surrounded by a liquid film. The thickness of the liquid film was constant, and the evaporation and condensation of the liquid film were ignored. The second-generation models were used to study the effect of different parameters (e.g. heat transfer distance

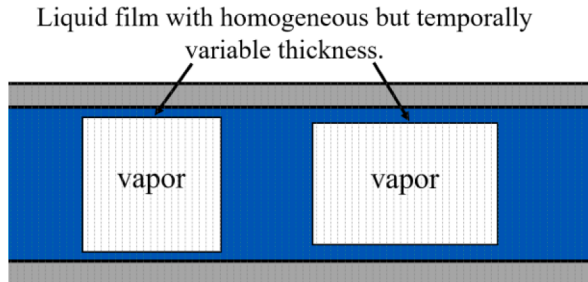
**Table 1**

Development in previous self-programming numerical models of PHPs.

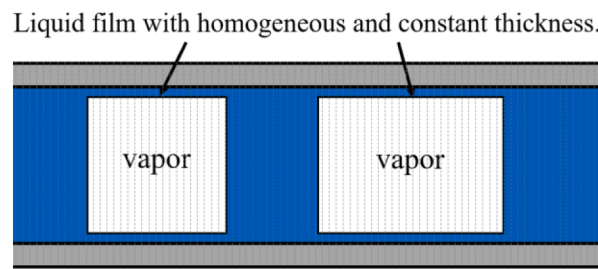
Literatures	Model's feature			Comments
	Heat transfer	Flow dynamics	Film dynamics	
Gen-1 Shafii et al [13] Manzoni et al [18]	The evaporation of liquid film was neglected.	Internal friction and capillary force were ignored.	Liquid film was not considered.	A one-dimensional simulation model of PHP was first developed. Homogeneous and heterogeneous condensation/evaporation in the PHP was first considered.
				The model numerically reproduced the thermal cycle.
Gen-2 Daimaru et al. [19] Nekrashevyc et al [20] Bao et al [14] Sun et al [15]	The phase change didn't affect the volume and mass of the liquid slugs. Heat transfer was calculated by film evaporation/condensation model with heat conduction.	Internal friction and capillary force were ignored.	Liquid film with homogeneous and constant thickness.	The model preliminarily simulated the operational shutdown of PHPs due to dry-out.
	The evaporation of liquid film was neglected.	Internal friction was ignored.		The model reproduced the transient flow and heat transfer for different adiabatic section lengths
	The state of vapor was calculated by Redlich-Kwong-Soave equation .	Surface tension was ignored.		The model for cryogenic PHPs was first established.
	Phase change heat transfer was calculated by a fixed bubble generation rate.	Capillary force was ignored.	Liquid film with homogeneous but temporally variable thickness.	The error margin between experiment and simulation is $\pm 13\%$ .
Gen-3 Sakulchangsatjatai et al [21] Mameli et al [16]	The evaporation of liquid film was neglected.			The model considered the local pressure losses caused by the existence of turns at the first time.
	Heat exchange between the wall and the working fluid was neglected.	Only fully developed flow was considered.	Liquid film varied with time and space, but the liquid film was assumed to have a linear temperature profile.	The model was established based on the model of Bae et al. [9] and improved by the lumped parameter approach to save computational time.
Gen-4 Noh et al [17] Present study	Both nucleate boiling and evaporation of liquid film were considered.	The effects of driving force, internal friction and capillary force were analyzed.	Liquid film varied with time and space, and was calculated by mass and energy conservation equation.	A comprehensive numerical model for different working conditions was proposed.



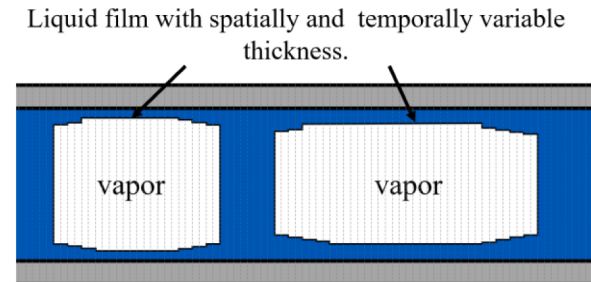
(a) First-generation model



(c) Third-generation model



(b) Second-generation model



(d) Fourth-generation model (present model)

Fig. 1. Development of models based on liquid film dynamics.

[14], working fluid [15]) on the operational performance of PHPs. Introducing a fixed-thickness liquid film into the theoretical model can cause deviations between the modeled and actual heat and mass transfer processes. To address these limitations, third-generation models were proposed. The third-generation models assumed that the thickness of the

liquid film was spatially uniform but temporally variable, as proposed by Mameli et al. [16]. These made it possible to investigate the dry-out phenomenon in PHPs. However, due to the evaporation of liquid film, the thickness of the liquid film varies simultaneously with time and space in actual operation. Noh et al. [17] have built theoretical models

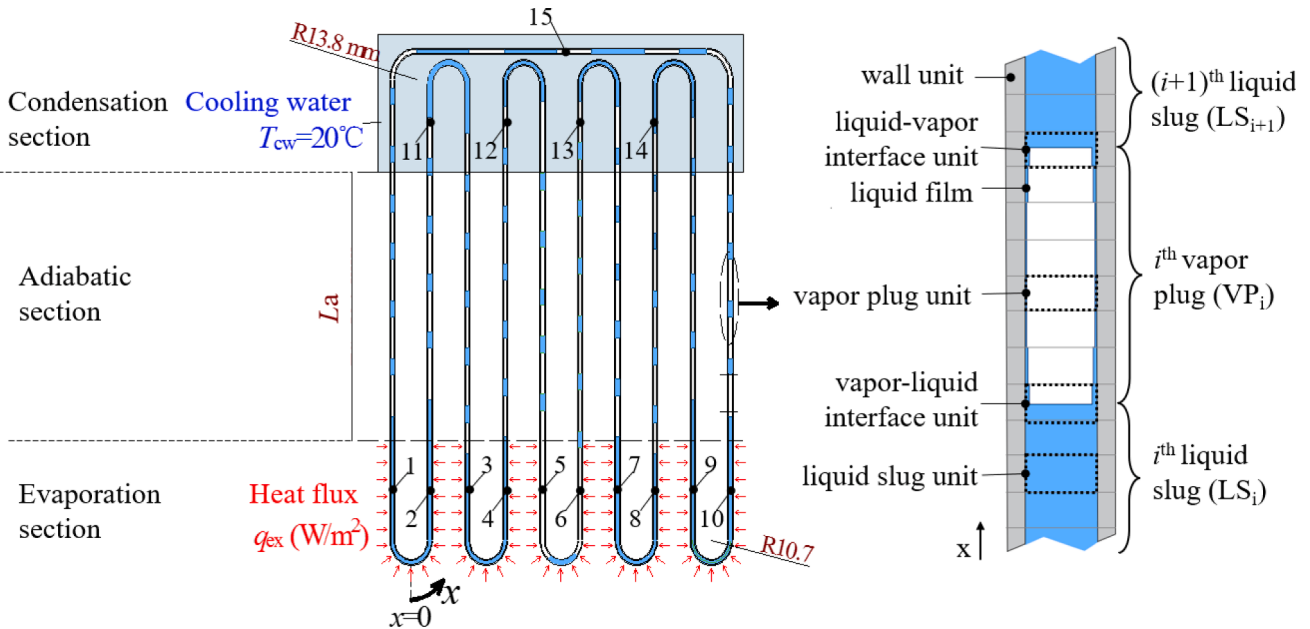


Fig. 2. Physical model and internal control units of the PHP.

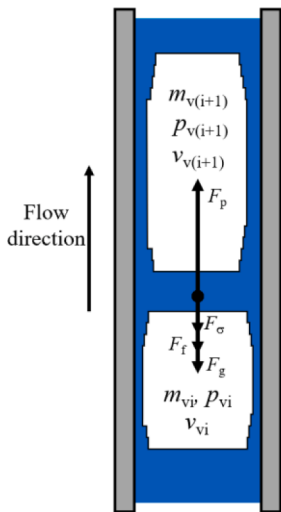


Fig. 3. Forces acting on the liquid slug.

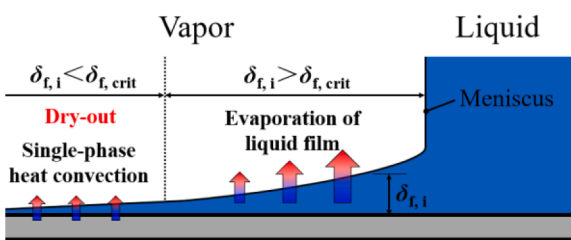


Fig. 4. The heat transfer mechanism between the wall and the vapor plug.

to reproduce this process. However, the heat transfer process in the liquid film was simplified in the model of Noh et al. [17], which affected the accurate assessment of the heat transfer performance of the PHP. Therefore, although significant advancements have been made in related theoretical studies, there are still several deficiencies that require further development and refinement.

For the experimental research, Czajkowski et al [22] analyzed the

influence of three varied adiabatic section lengths on the operation characteristics of PHPs and noticed that the heat transfer capacity at elevated heat input was enhanced with the growth of the adiabatic section length. The experimental findings of Czajkowski et al [22] showed that a shorter adiabatic section length improved the start-up of PHPs and shortened the start-up time. Ara et al [23] carried out a study about the operation performance of the PHP under a large heat transfer distance in a solar thermal collector. It was found that in the range of 0.6~1.6 m adiabatic section length, a reduction in length resulted in a decrease in the flow resistance of working fluid, which made the oscillating frequency higher. The higher oscillating frequency was conducive to the heat transfer capacity of the PHP, leading to a smaller thermal resistance. Shi et al. [24] evaluated the heat transfer performance of nitrogen-PHPs with varying pipe structures and heat transfer distances. The nitrogen-PHP demonstrated a strong long-distance heat transfer capacity, with a maximum heat transfer coefficient of 166,400 W/(m·K). Liu et al. [25] conducted a visualization experiment. The results indicated that stagnation was more probable in the water-PHP under a large heat transfer distance during operation. The stagnation and reactivation of the working fluid exacerbated the evaporating temperature fluctuation, which influenced the steady-state operation of the PHP. Experimental results also proved that as the increase of heat transfer distance was extended, the start-up, flow and heat transfer performance gradually deteriorated, but the anti-dry-out capability initially increased and subsequently decreased.

In summary, an accurate simulation of the operational performance of PHPs at varying heat transfer distances remains challenging. The impact of heat transfer distance on the flow and heat transfer performance of PHPs has not been revealed in the previous research. These limitations hinder the further application of PHPs. Therefore, a two-phase heat and mass transfer model incorporating liquid film dynamics was established and partial visualization experiments were conducted to validate the reliability of the theoretical model. Based on these, the flow and heat transfer performance of R1336mzz(Z)-PHPs under various heat transfer distances were numerically simulated and experimentally investigated. The flow and heat transfer characteristics of R1336mzz(Z)-PHPs were compared with those of water-PHPs and ethanol-PHPs to investigate the influence of working fluids on the operating performance of PHPs through numerical simulation. The study achieved accurate predictions of the flow and heat transfer

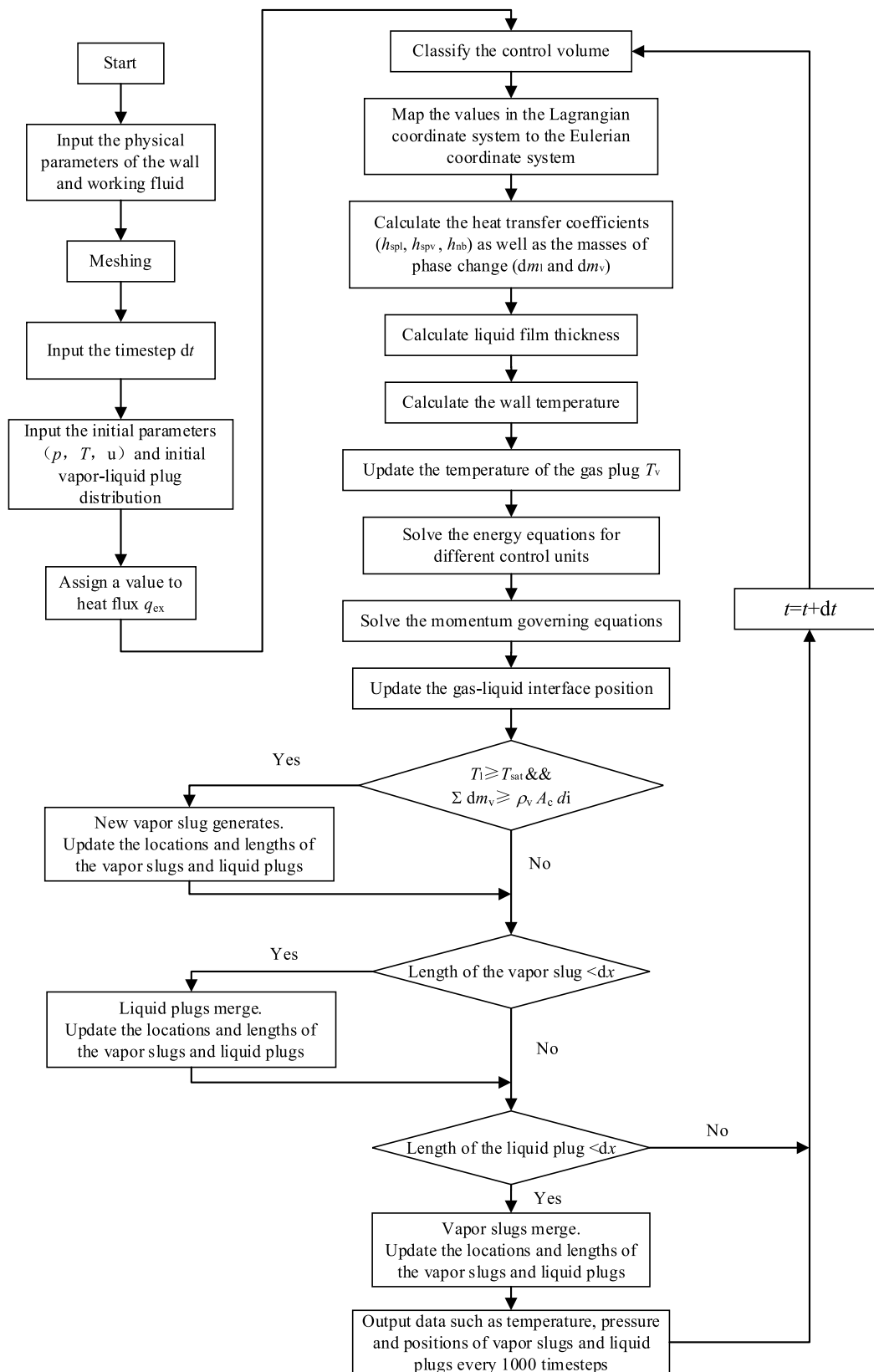


**Fig. 5.** Numerical calculation process of the theoretical model.

performance of PHPs and provided experimental and theoretical support for the application of PHPs at varying heat transfer distances.

## 2. Two-phase heat transfer model incorporating liquid film dynamics

Previous studies on the heat transfer characteristics of PHPs have

**Table 2**  
Input parameters of the theoretical model.

Parameter	Value
Heat transfer distance $L_a$ (mm)	130, 500, 1000, 1500
Evaporation section length $L_e$ (mm)	60
Condensation section length $L_c$ (mm)	65
Inclination angle ( $^\circ$ )	90
Heat input $Q$ (W)	20, 40, 60, 80, 100
Area of the evaporation section ( $\text{m}^2$ )	$6.157 \times 10^{-3}$
Filling ratio	0.5
Coolant temperature $T_\infty$ ( $^\circ\text{C}$ )	20
Timestep (s)	$5 \times 10^{-5}$

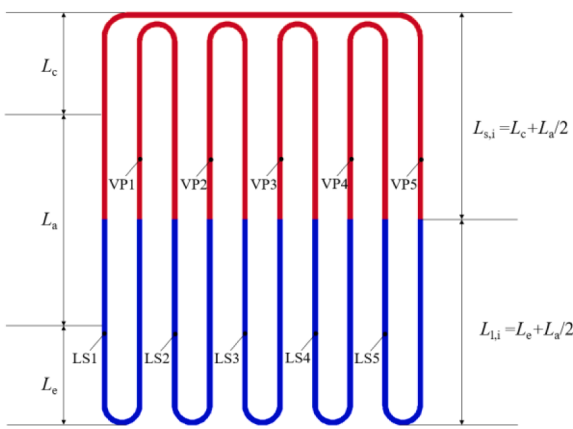


Fig. 6. Initial state of two-phase flow distribution.

often overlooked the impact of liquid film dynamics. The assumption of a constant film thickness during numerical simulations has hindered the accurate representation of the local dry-out phenomenon during operation. To address this limitation and provide a more accurate prediction of the PHP's performance, a two-phase heat and mass transfer model incorporating liquid film dynamics was developed based on the theoretical work of Bao et al. [14].

### 2.1. Main assumptions of the heat transfer model for PHP

Fig. 2 showed a sketch of the physical model and the internal control units. Numbers 1–15 in Fig. 2 represented 15 measurement points.

The primary assumptions of the heat transfer model are given below:

- (1) The fluid was presumed to be incompressible and the vapor was regarded as ideal gas;
- (2) Pressure and temperature were assumed to be uniformly distributed within a single vapor plug;
- (3) The shear stress between the vapor plugs and the liquid film was neglected;
- (4) The liquid film was assumed to be supplied by adjacent liquid slugs and adhere to the wall. The thickness of the liquid film changed as the evaporation and condensation occurred;
- (5) The liquid phase density was presumed to be a constant at  $20\text{ }^\circ\text{C}$ , and the remaining key thermal properties (viscosity, surface tension, specific heat capacity, thermal conductivity, and latent

heat of vaporization) were calculated based on saturation state values at the corresponding temperatures.

- (6) Flow motion of the working fluid in the PHP was assumed to be slug flow.

### 2.2. Establishment of the heat transfer model

#### 2.2.1. Energy governing equations

##### (1) Energy governing equation for the wall unit

The energy governing equation for the wall is presented below:

$$(\rho_w A_w dx) c_{pw} \frac{dT_{w,j}}{dt} = \lambda_w A_w \frac{\partial T_{w,j}}{\partial x} + q_{ex} (\pi d_{in} dx) - q_{wf,j} (\pi d_{in} dx) \quad (1)$$

Where, the heat flux of the wall ( $q_{ex}$ ) is determined by:

$$q_{ex} = \begin{cases} q & : \text{evaporation section} \\ 0 & : \text{adiabatic section} \\ h_c (T_{cw} - T_\infty) & : \text{condensation section} \end{cases} \quad (2)$$

Where,  $h_c = Nu_{cw} \times \lambda_l / d_o$ , and  $Nu_{cw}$  is calculated by [26]:

$$Nu_{cw} = 0.3 + \frac{0.62 Re^{1/2} Pr^{1/3}}{\left[1 + (0.4/Pr)^{2/3}\right]^{1/4}} \left[1 + \left(\frac{Re}{282000}\right)^{5/8}\right]^{4/5} \quad (3)$$

The heat transfer between the liquid slug and the wall in the PHP can be mainly categorized into two types: single-phase convective heat transfer and boiling heat transfer. The onset of nucleate boiling is determined by [27]

$$\Delta T_{sat,crit} = \left( \frac{8\sigma T_{sat,l} q}{h_{fg} \rho_{sat} \lambda_l} \right)^{1/2} \quad (4)$$

When  $(T_w - T_{sat}(p_l)) < \Delta T_{sat,crit}$ , liquid slugs transfer heat through single-phase convection process; when  $(T_w - T_{sat}(p_l)) \geq \Delta T_{sat,crit}$ , nucleate boiling occurs in the liquid slug. When nucleate boiling occurs, the total

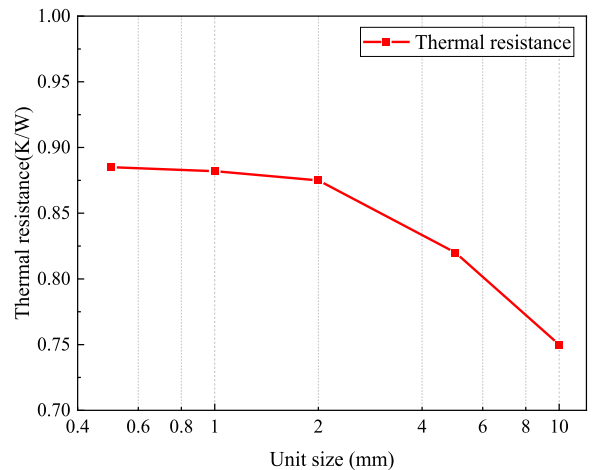
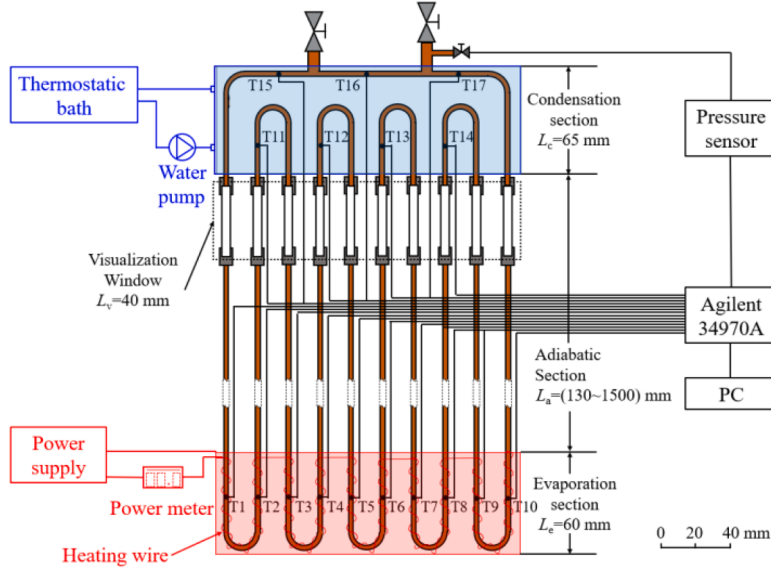


Fig. 7. Independency tests on unit size.

**Table 3**  
Comparison of key thermal properties of water, ethanol and R1336mzz(Z) ( $20\text{ }^\circ\text{C}$ ) [37].

Working fluid	$(dp/dT)_{sat}$ (Pa/K)	$\sigma$ (mN/m)	$\mu$ (mPa/s)	$h_{fg}$ (kJ/kg)	$c_p$ (kJ/kg·K)	$\lambda_l$ (mW/m·K)	$\theta_s$ ( $^\circ$ )
R1336mzz(Z)	11,306	15.491	0.364	168.54	1.2204	72.164	2
Ethanol	1411.1	21.948	1.081	920.66	2.4346	163.45	40
Water	612.93	71.97	0.8905	2437.3	4.183	609.44	85



**Fig. 8.** Experimental setup for PHPs at various heat transfer distances [38].

**Table 4**

Key parameters of the experimental setup.

Parameter	value
Heat transfer distance(mm)	130, 500, 1000, 1500
Visual window length (mm)	40
Evaporation section length (mm)	60
Condensation section length (mm)	65
Number of turns	5
Inner diameter (mm)	2
Outer diameter (mm)	3 (copper tubes) 6 (glass tubes)
Inclination angle ( $^{\circ}$ )	90

heat transfer can be considered as a combination of the single-phase convection heat transfer and nucleate boiling heat transfer. Therefore, the heat flux  $q_{wf}$  between the wall and the liquid can be computed by:

$$q_{wf} = \begin{cases} h_{spl}(T_w - T_1), T_w - T_{sat}(p_1) < \Delta T_{sat, crit}, & \text{heat transfer with liquid} \\ (h_{spl} + h_{nb})(T_w - T_1), T_w - T_{sat}(p_1) \geq \Delta T_{sat, crit}, & \text{heat transfer with liquid} \\ h_{spv}(T_w - T_v), & \text{heat transfer with vapor} \end{cases} \quad (5)$$

**Table 5**

Experimental operation conditions.

Condition	Value
Working fluid	R1336mzz(z)
Heat input (W)	10~100
Temperature of the cooling water ( $^{\circ}\text{C}$ )	20
Flow rate of the cooling water (L/min)	3
Vacuum (Pa)	< 2

Where, the convective heat transfer coefficient between the liquid plug and the wall is calculated by [28,29]:

$$h_{spl} = \begin{cases} \left(\frac{\lambda_l}{d_{in}}\right) \cdot 4.36 & : Re \leq 2000 \\ \left(\frac{\lambda_l}{d_{in}}\right) \cdot \left( \frac{(f_r/8)(Re_l - 10^3)Pr_l}{1 + 12.7(f_r/8)^{1/2}(Pr_l^{2/3} - 1)} \right)^{1/3} & : 2000 < Re \leq 10000 \\ \left(\frac{\lambda_l}{d_{in}}\right) \cdot 0.023Re_l^{0.8}Pr_l^{0.4} & : Re > 10000, \text{ evaporation and adiabatic sections} \\ \left(\frac{\lambda_l}{d_{in}}\right) \cdot 0.023Re_l^{0.8}Pr_l^{0.3} & : Re > 10000, \text{ condensation section} \end{cases} \quad (6)$$

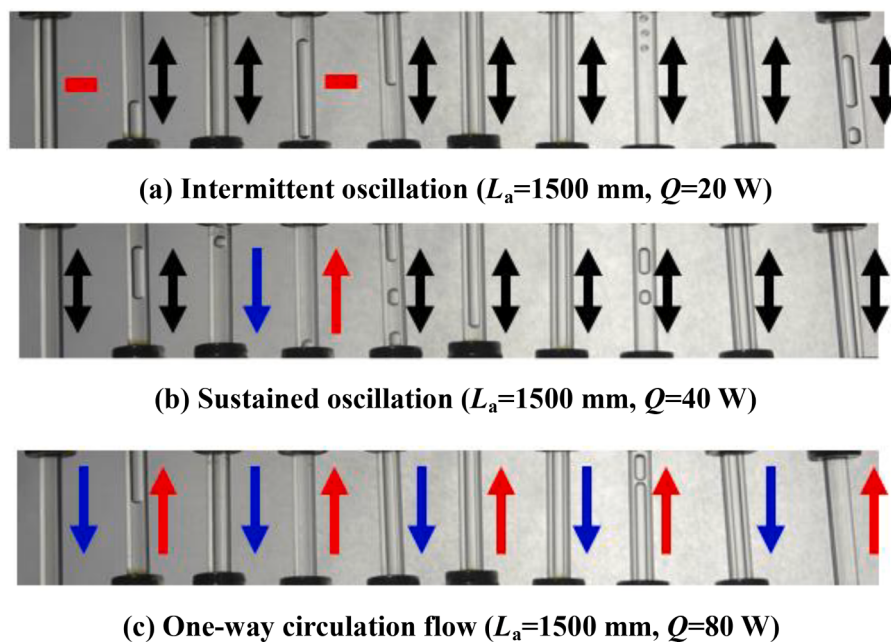


**Fig. 9.** Flow states of R1336mzz(Z) during steady-state operation in the experiment.

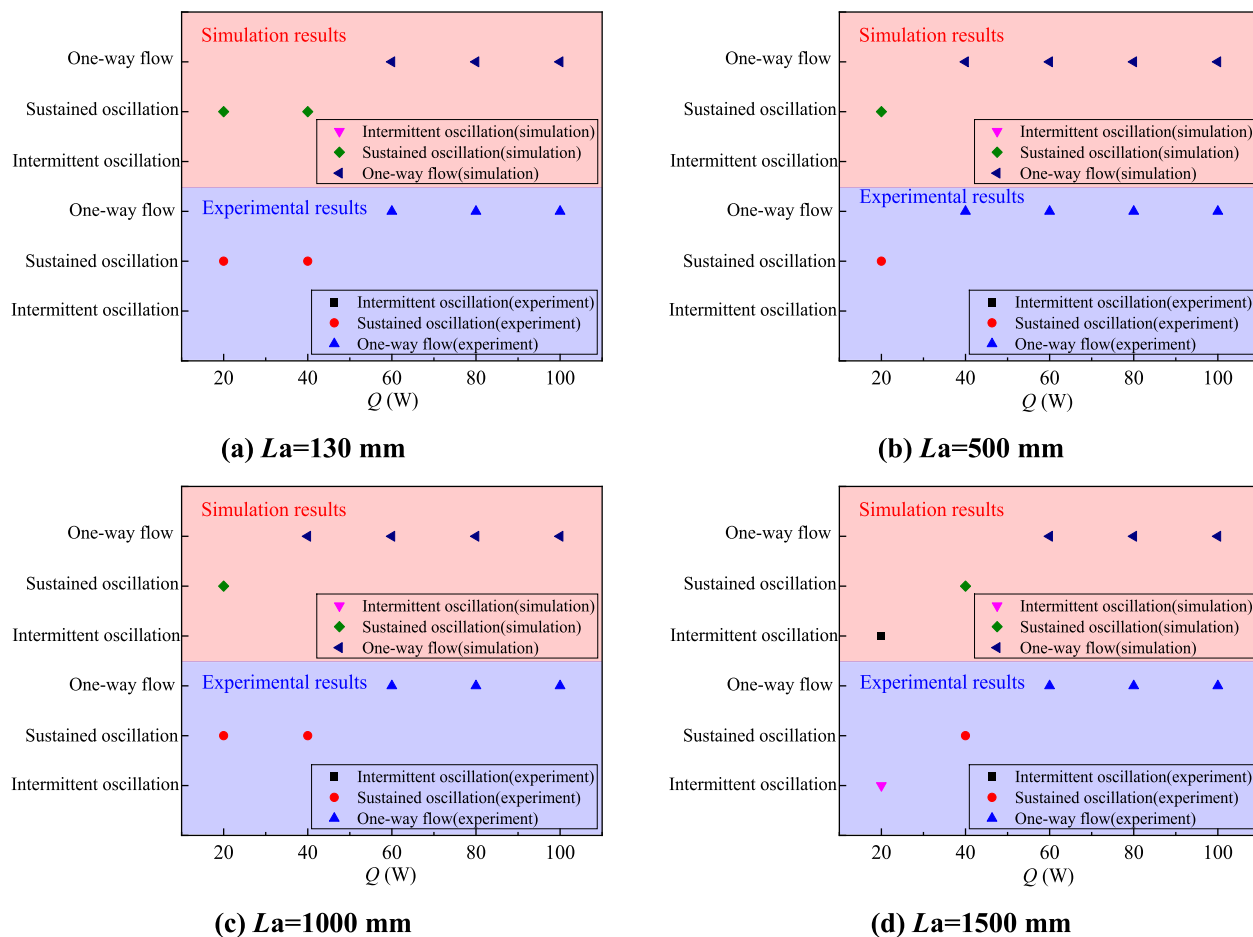


**Fig. 10.** Comparison of the theoretical and experimental flow states during steady-state operation.

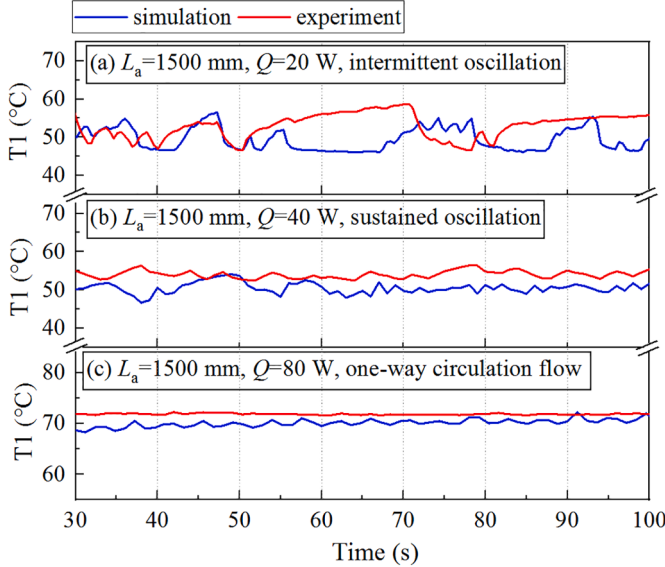


**Fig. 11.** Comparison of the transient temperature during steady-state operation at measurement point 1.

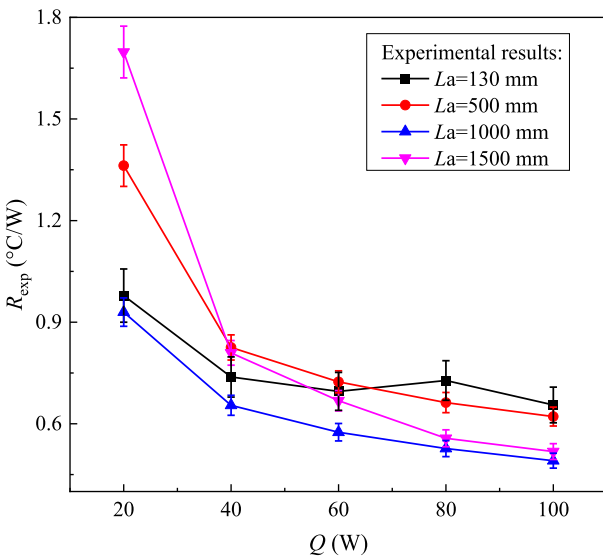


**Fig. 12.**  $R_{\text{exp}}$  vs.  $Q$ .

The boiling heat transfer coefficient  $h_{\text{nb}}$  can be calculated by [30]:

$$h_{\text{nb}} = 0.00122 \left[ \frac{\lambda_l^{0.79} c_{pl}^{0.45} \rho_l^{0.49}}{\sigma^{0.5} \mu^{0.29} h_{fg}^{0.24} \rho_v^{0.24}} \right] [T_w - T_{\text{sat}}(p_l)]^{0.24} [p_{\text{sat}}(T_w) - p_l]^{0.75} S \quad (7)$$

Where  $S$  is the nucleate boiling suppression factor, calculated by the correlation equation proposed by Bennett et al. [31].

The convective heat transfer coefficient  $h_{\text{spv}}$  between the wall and the vapor plug is determined by [26]:

$$h_{\text{spv}} = 4.36 \lambda_v / d_{\text{in}} \quad (8)$$

In addition, during the nucleate boiling process, the mass of the phase change is calculated by:

$$dm_l = h_{\text{nb}} A_l [T_w - T_{\text{sat}}(p_l)] / h_{fg} \quad (9)$$

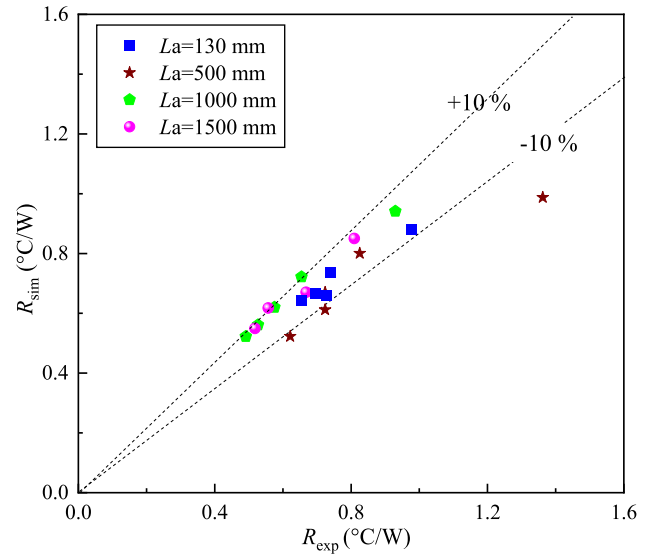


**Fig. 13.** Comparison of  $R_{\text{exp}}$  and  $R_{\text{sim}}$ .

**Table 6**  
Operating parameters of experimental/theoretical cases used for validation.

Literature	Bea et al. [9]	Mameli et al. [16]	Liu et al. [38]	This work
$d_i / d_o$ (mm)	1/1.6	2/3	2/3	2/3
$L_a$ (mm)	100	220	130	130
$L_e$ (mm)	200	30	60	60
$L_c$ (mm)	300	40	65	65
Number of turns	2	2	5	5
Orientation	vertical	vertical	vertical	vertical
Filling ratio	0.65	0.65	0.5	0.5
Tube material	stainless steel	copper	copper	copper
Working fluid	ethanol	ethanol	ethanol	ethanol
Heat input (W)	50–100	50–100	10–100	20–100
condenser temperature (°C)	15	15	20	20

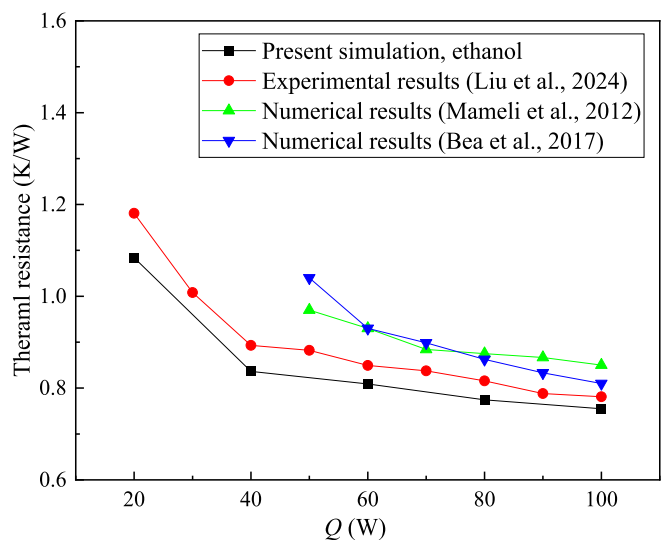


**Fig. 14.** Comparison of  $R$  obtained from the present study with those in the literatures.

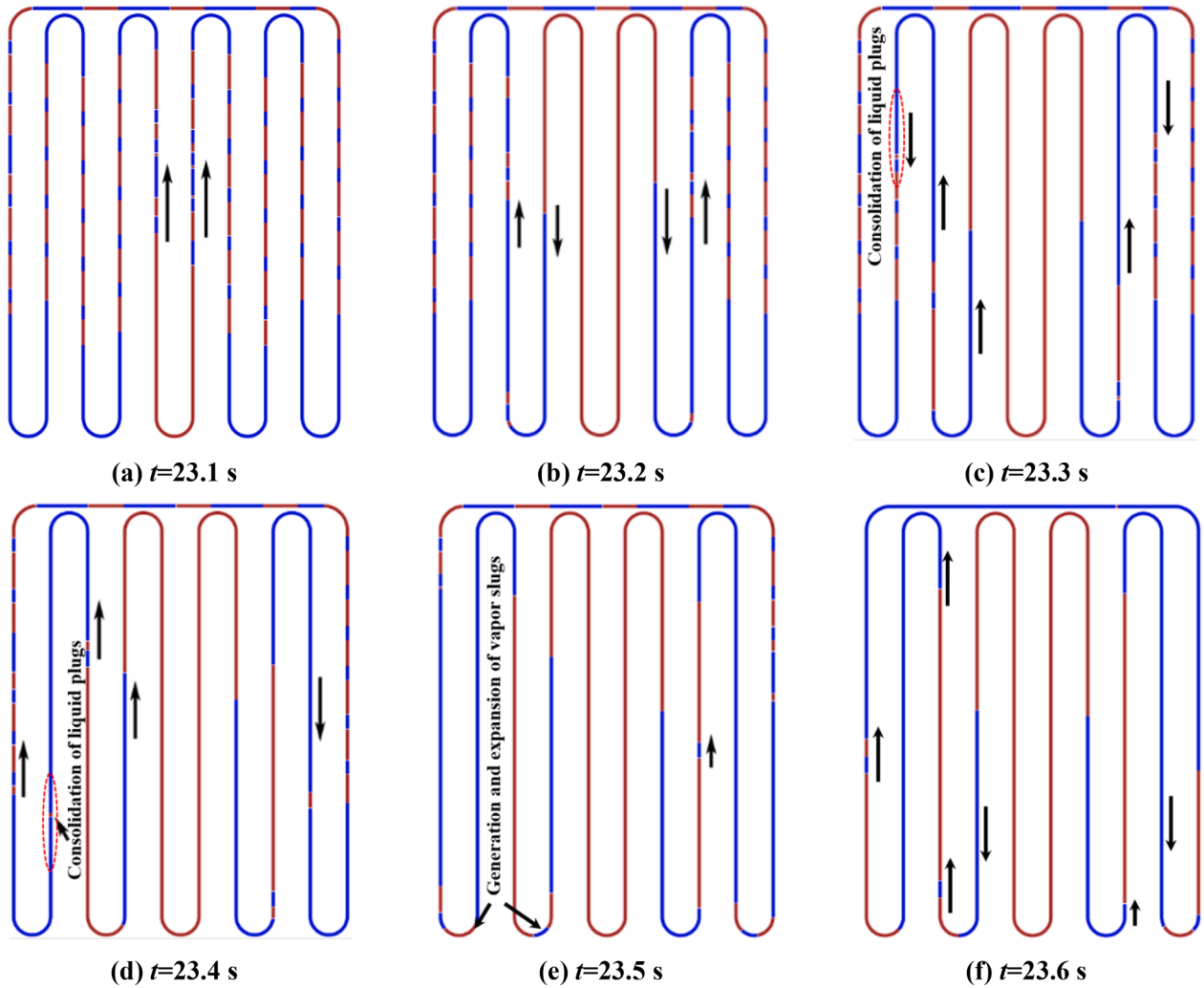


**Fig. 15.** Flow states of R1336mzz(Z) in PHPs during simulation ( $L_a=130$  mm,  $Q = 20$  W). Blue indicated liquid slugs, red indicated vapor plugs, and the direction of arrows indicated the direction of movement of the working fluid)

#### (2) Energy governing equation for the liquid slug unit

The energy governing equation for the liquid slug is calculated by

$$(\rho_l A_{cr} dx) c_{pl} \frac{dT_l}{dt} = \lambda_l A_{cr} \frac{\partial T_l}{\partial x} + q_{wf} (\pi d_{in} dx) \quad (10)$$

$$dT_v = \frac{\sum_i h_v A_i (T_{w,j} - T_v) + R_g T dm_v - pdV}{m_v c_v} \quad (12)$$

The pressure inside the vapor plug is obtained by:

$$p_v = (m_v R_g T_v) / V_v \quad (13)$$

Where, the left side of the equation represents the variation of the liquid slug's energy with time; the first term on the right side of the equation is the heat transfer by axial thermal conductivity of the liquid slug; and the second term on the right side is the heat transfer by heat transfer from the wall to the liquid slug.

#### (3) Energy governing equation for the vapor plug unit

The energy governing equation for the vapor plug is calculated by:

$$\frac{dm_v c_{vv} T_v}{dt} = \sum_i h_v A_i (T_{w,j} - T_v) + c_{pv} T_v \frac{dm_v}{dt} - p \frac{dV}{dt} \quad (11)$$

Based on the ideal gas assumption, Meyer's formula ( $c_{pv}-c_{vv}=R_g$ ) is introduced to Eq. (11):

#### (4) Energy governing equation for the liquid-vapor interface unit

Since the energy change of the vapor plug in the interface unit is much smaller than that in the vapor plug unit, the energy change of the vapor plug in the interface unit is ignored. For the liquid slug in the interface unit, the thermal conductivity between the liquid slug and vapor plug is much smaller than that inside the liquid plug and the heat transfer due to phase change at liquid-vapor interface is much smaller than the heat transfers due to evaporation of the thin liquid film and nucleate boiling of the liquid slug [17]. Therefore, the thermal conductivity between the liquid slug and vapor plug and the heat transfer due to phase change at liquid-vapor interface are neglected. The energy governing equation for the liquid slug in liquid-vapor interface unit can be expressed as:

$$\frac{\partial m_l c_{pl} T_l}{\partial t} = -\frac{\partial T_l}{\partial x} \lambda_l A_{cr} + q_{wf} \pi d_{in} x_l - \frac{dm_l}{dt} c_{pl} T_l \quad (14)$$

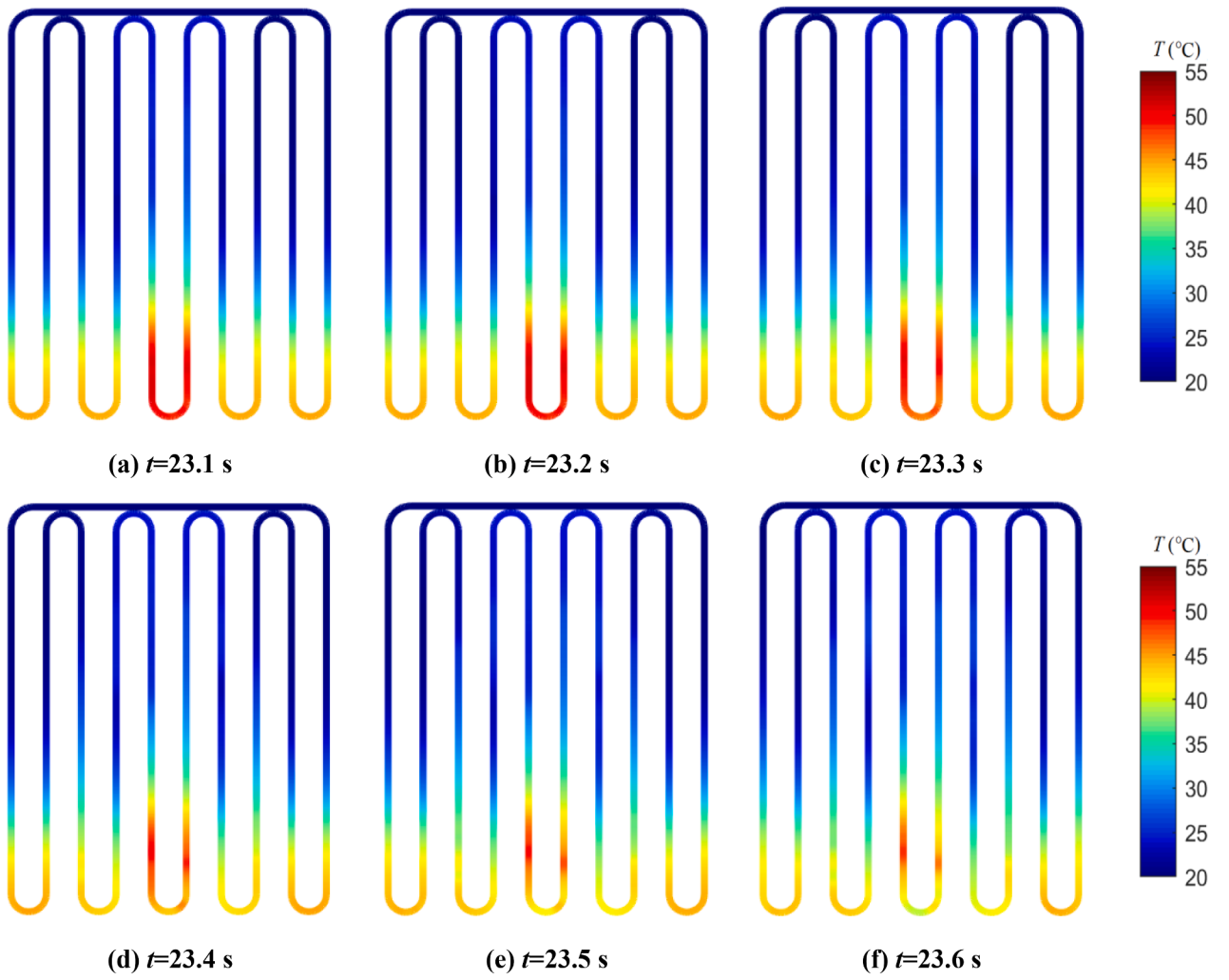


Fig. 16. Variation of temperature with time during operation in R1336mzz(Z)-OHPs ( $L_a=130$  mm,  $Q = 20$  W).

### 2.2.2. Mass and momentum governing equations

The forces acting on the liquid slug in the PHP include the driving force  $F_p$ , gravity  $F_g$ , internal friction  $F_f$ , and capillary force  $F_\sigma$ , as exhibited in Fig. 3.

The effect of the forces on the movement of the liquid slug can be calculated by:

$$\frac{dm_{li}v_{li}}{dt} = F_p - F_f - F_\sigma - F_g \quad (15)$$

where the driving force  $F_p$  is computed based on the pressure difference between the vapor plugs at each end of the liquid slug:

$$F_p = (p_{vi} - p_{v(i+1)})A_c \quad (16)$$

The internal friction  $F_f$  is calculated as follows [32]:

$$F_f = \frac{f_t}{2d_{in}} L e_i \rho_l u_i^2 \quad (17)$$

where  $f_t$  and  $\Delta p_f$  are calculated according to the empirical correlation equations [32]:

$$f_t = \begin{cases} 64/Re_l & , Re_l < 2000 \\ 0.3164 Re_l^{-0.25} & , Re_l \geq 2000 \end{cases} \quad (18)$$

$$\Delta p_f = \frac{\rho_l u_i^2}{2} \left( \frac{f_t L e_i}{d_i} + K \right) \quad (19)$$

$$K = \left[ 0.131 + 0.1632 \left( \frac{d_{in}}{R_{turn}} \right)^{3.5} \right] \quad (20)$$

The capillary force  $F_\sigma$  is calculated as follows:

$$F_\sigma = \pi d_{in} \sigma (\cos \theta_{rc} - \cos \theta_{ac}) \quad (21)$$

where  $\theta_{rc}$  and  $\theta_{ac}$  can be calculated from the capillary number and static contact angle [33]:

$$\cos \theta_{ac} = \cos \theta_s - 2(1 + \cos \theta_{sc}) Ca^{0.5} \quad (22)$$

$$\theta_{rc} = \theta_s - 0.5(\theta_{ac} - \theta_{rc}) \quad (23)$$

The gravity is calculated as follows:

$$F_g = \sum_i \rho g A_{cr} dx \cos \beta \quad (24)$$

During the operation, the generation and merging of liquid slugs and vapor plugs may occur in the PHP, corresponding to the following mass and momentum governing equations:

#### (1) Merging of liquid slugs

When the length of the vapor plug between two liquid slugs is less than the unit size, the two slugs will merge to form a new liquid slug, and the vapor plug will disappear. The corresponding mass and momentum conservation equations are as follows:

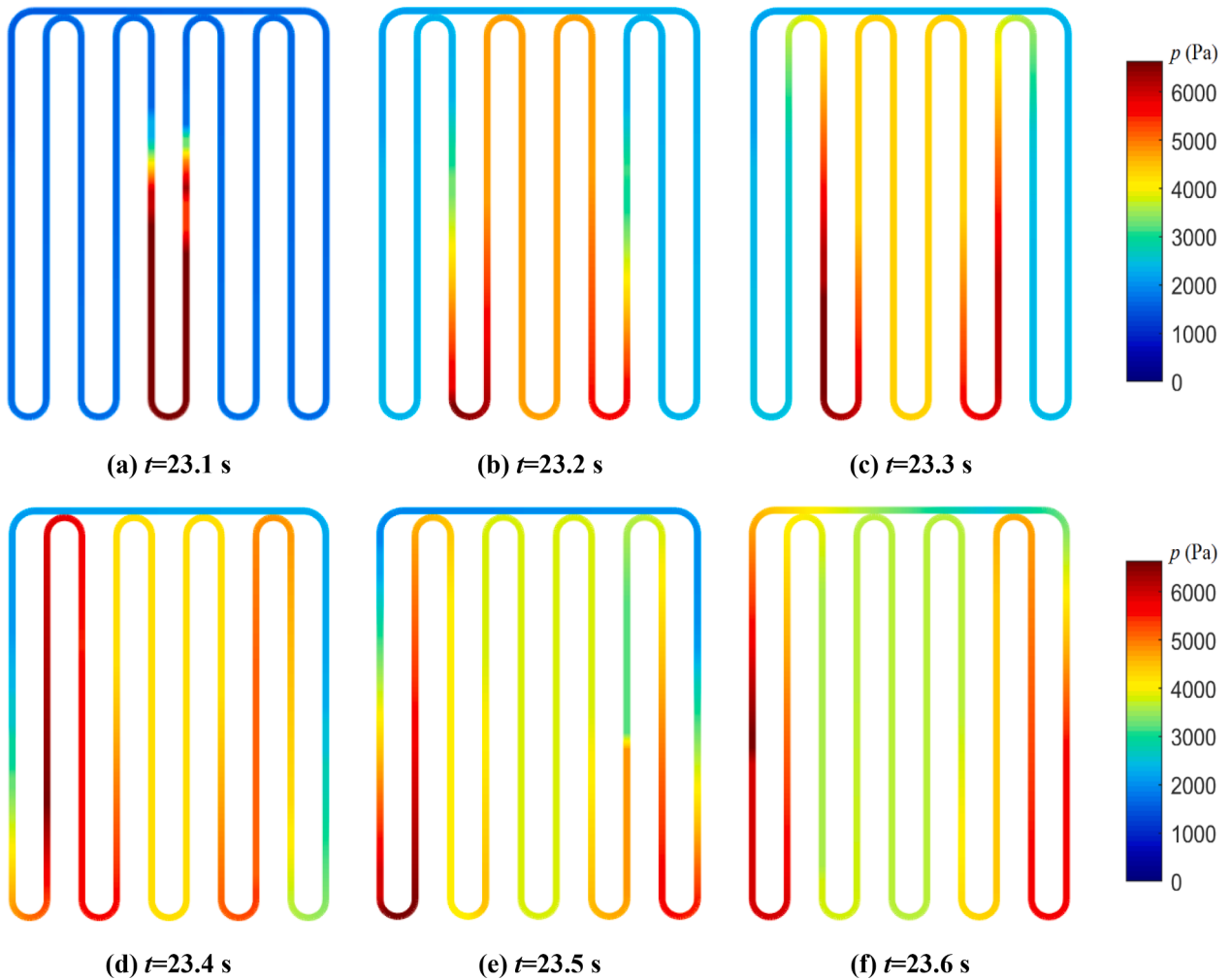


Fig. 17. Variation of pressure with time during operation in R1336mzz(Z)-PHPs ( $L_a=130$  mm,  $Q = 20$  W).

$$m_{\text{new}} = m_{\text{left}} + m_{\text{right}} \quad (25)$$

$$m_{\text{new}}v_{\text{new}} = m_{\text{left}}v_{\text{left}} + m_{\text{right}}v_{\text{right}} \quad (26)$$

#### (2) Merging of vapor plugs

When the length of the liquid slug between two vapor plugs is less than the unit size, the two plugs will merge to form a new vapor plug. The corresponding conservation equations are as follows:

$$m_{\text{new}} = m_{\text{left}} + m_{\text{right}} \quad (27)$$

$$m_{\text{new}}c_{\text{v,v}}T_{\text{new}} = m_{\text{left}}c_{\text{v,v}}T_{\text{left}} + m_{\text{right}}c_{\text{v,v}}T_{\text{right}} \quad (28)$$

$$V_{\text{new}} = V_{\text{left}} + V_{\text{right}} \quad (29)$$

$$P_v = \frac{m_{\text{new}}R_g T_{\text{new}}}{V_{\text{new}}} \quad (30)$$

#### (3) Generation of new vapor plugs

When the size of the bubbles produced by the nucleate boiling of the liquid slug approaches the inner diameter of the tube ( $dm_l > \rho_v A_c d_i$ ), a new vapor plug is generated. The temperature, volume, pressure and mass of the new vapor plugs are as follows:

$$m_v = dm_l \quad (31)$$

$$T_v = T_l = T_{\text{sat}}(p_l) \quad (32)$$

$$p_v = p_{\text{sat}}(T_v) \quad (33)$$

$$V_v = m_v R_g T_v / p_v \quad (34)$$

#### (4) Generation of new liquid slugs

When the thickness of the liquid film is broader than or equal to the capillary radius, a new plug is produced, and the mass and temperature of the new plug are as follows

$$m_l = m_f \quad (35)$$

$$T_l = T_f \quad (36)$$

#### 2.2.3. Liquid film dynamics

The heat transfer mechanism between the wall and the vapor plug in the PHP is related to the phase change of the liquid film, as shown in Fig. 4. When the liquid film thickness  $\delta_f$  is smaller than the critical thickness  $\delta_{f,\text{crit}}$ , the liquid film can be regarded as dry-out state. At this time single-phase convection heat transfer occurs. The convection heat transfer is calculated as shown in Eqs. (5) and (7). When the liquid film thickness exceeds the critical thickness  $\delta_{f,\text{crit}}$ , the phase change of the liquid film dramatically improves the heat transfer coefficient. The

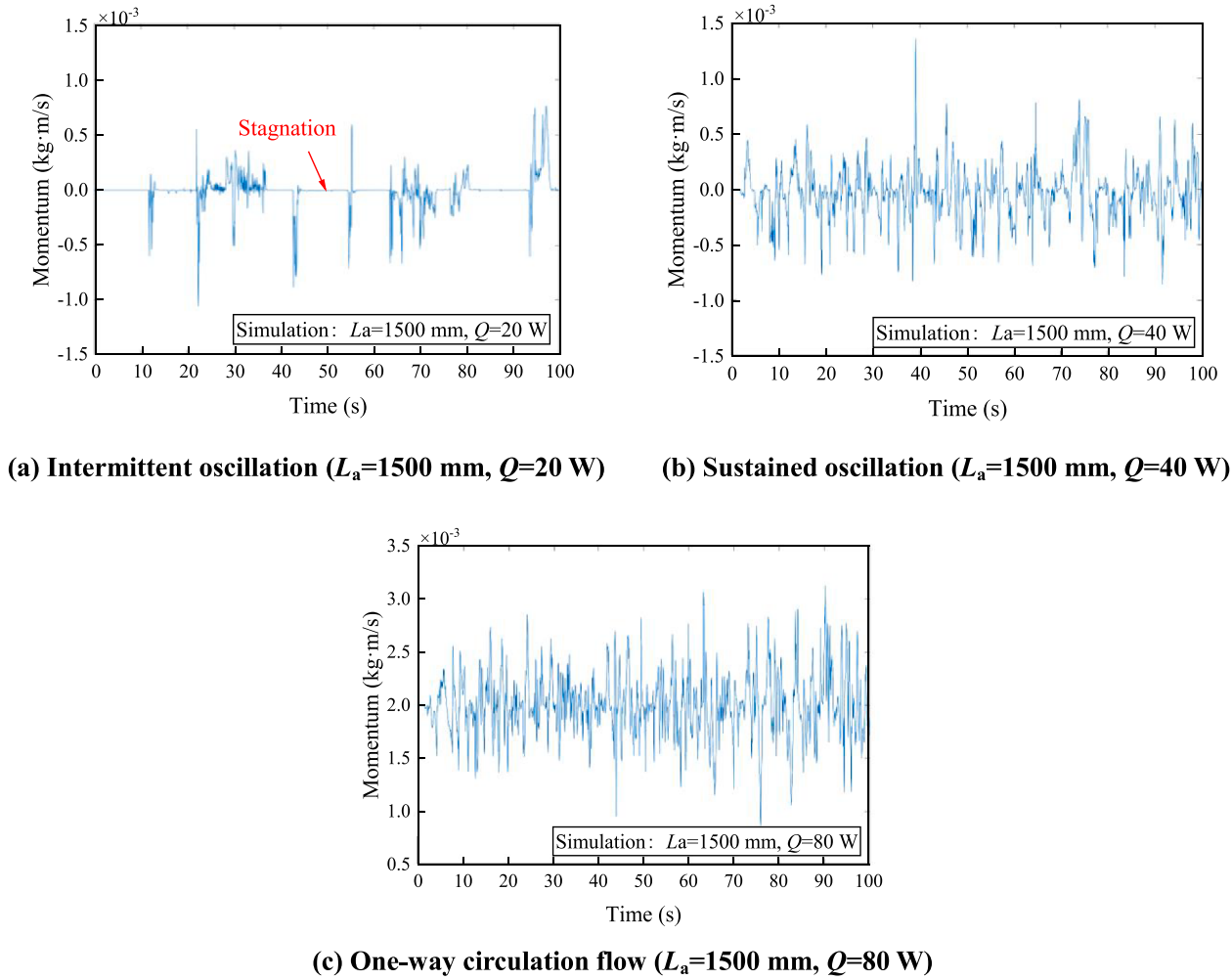


Fig. 18. Three typical flow states in R1336mzz(Z)-PHPs.

critical liquid film thickness was related to the thermophysical properties of the working fluid and the surface roughness of the PHPs' material, which was mainly determined based on the typical experimental data [34].

The heat flux exchanged between the wall and the liquid film is determined as below:

$$q_{wf} = \lambda / \delta_f (T_w - T_f) \quad (37)$$

where the liquid film thickness  $\delta_f$  is calculated based on the initial thickness  $\delta_{f0}$  and the liquid film mass governing equation. The initial thickness is determined using the following equation [17,35]:

$$\delta_{f0} = \begin{cases} 0.67 Ca^{2/3} \times d_{in}, & Re \leq 50 \\ \frac{0.67 \times Ca^{2/3} \times d_{in}}{1 + 3.13 Ca^{2/3} + 0.504 Ca^{0.672} Re^{0.589} - 0.352 We^{0.629}}, & 50 < Re \leq 2000 \\ \frac{0.67 \times Ca^{2/3} \times d_{in}}{1 + 3.13 Ca^{2/3} + 44.33 Ca^{0.672} - 41.96 Ca^{0.629}}, & Re \geq 2000 \end{cases} \quad (38)$$

where,

$$Ca = \mu u / \sigma \quad (39)$$

$$We = Re \times Ca \quad (40)$$

When the liquid film undergoes an evaporation or condensation

phase change, its thickness  $\delta_f$  varies with time and is calculated according to the liquid film mass governing equation:

$$\rho_l \pi (d_{in} - 2\delta_f) dx \frac{d\delta_f}{dt} = \frac{dm_v}{dt} \quad (41)$$

where,

$$\frac{dm_v}{dt} = (q_{fi} - q_{gi}) A_f / h_{fg} \quad (42)$$

$$q_{fi} = \lambda_1 / \delta_f (T_f - T_{fi}) \quad (43)$$

$$q_{gi} = h_{spv} (T_f - T_v) \quad (44)$$

where, the liquid film evaporates when  $dm_v > 0$ ; the vapor plug condenses when  $dm_v < 0$ .  $T_f$  is the liquid film's temperature, which is calculated by:

$$\frac{\partial m_f c_{pl} T_f}{\partial t} = \lambda_i A_{cr,f} \frac{\partial T_f}{\partial x} + q_{wf} A_i - q_{fi} A_{fi} - dm_f c_{pl} (T_f - T_{sat,v}) \quad (45)$$

### 2.3. Numerical calculation process of the theoretical model

The simulations were carried out on the MATLAB platform and Fig. 5 demonstrated the calculation process of the theoretical model in this paper.

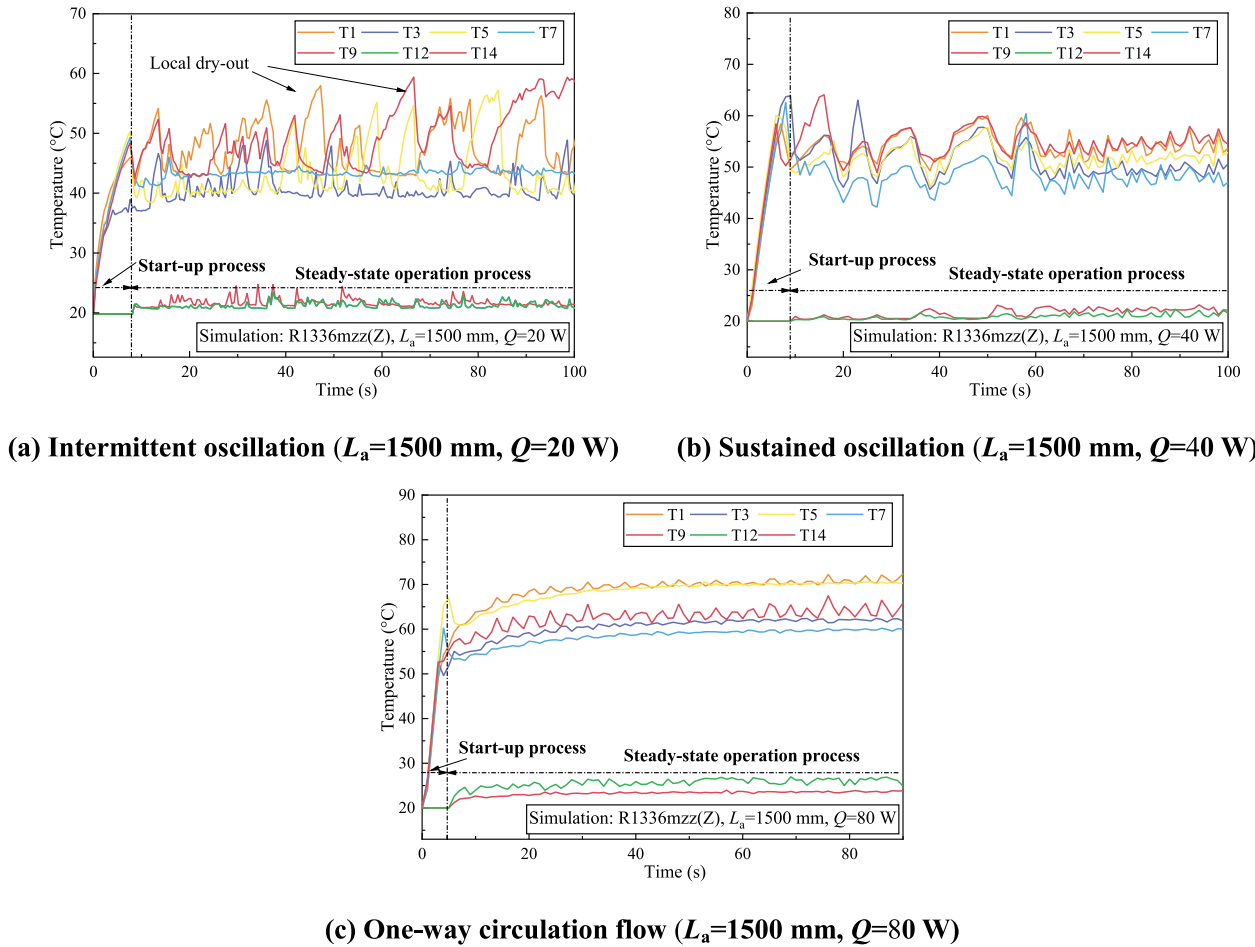


Fig. 19. Temperature fluctuations under three typical flow states.

#### 2.4. Input parameters of the numerical simulation

After discretizing the mass, energy and momentum governing equations by self-programming in the Matlab platform, the theoretical model was initialized according to the parameters of the relevant variables enumerated in Table 2. The initial state of the two-phase flow distribution was displayed in Fig. 6. To ensure that the numerical simulation results were both physically meaningful and easily verifiable through experiments, the dimensions and initial working conditions of the physical model were mainly designed based on the geometrical dimensions and common actual working conditions in previous experimental setups of PHPs. The initial temperature of the working fluid was 20 °C and the initial pressure in the PHP was 2kPa. The simulation parameters encompassed a range of heat inputs and heat transfer distances to evaluate the applicability of PHPs across different application scenarios. To guarantee the steady-state operation of PHPs in the simulation, a maximum heat transfer distance of 1500 mm was selected. This choice was based on findings from the previous study [25], which identified 1500 mm as the limiting heat transfer distance for water-based PHPs. In addition, the time step in the theoretical calculations was set to  $5 \times 10^{-5}$  s, which helped to effectively capture the dynamic behavior of the fluid while maintaining both the accuracy and stability of the numerical solution.

In the numerical simulation, R1336mzz(Z), water and ethanol were chosen as the working fluid of PHPs. The thermal properties were shown in Table 3. Water is the most extensively researched working fluid for PHPs. Compared with other pure fluids, water has a comparatively low  $(dp/dT)_{sat}$ , as well as high viscosity and surface tension, contributing to its inferior flow performance. At the same time, due to its comparatively

high specific heat capacity, thermal conductivity, and latent heat of vaporization, water has a strong heat transfer capability at high heat input. Therefore, in this study, water was chosen as a representative working fluid with poor flow properties but high heat transfer capacity (at the same heat input). R1336mzz(Z) is an eco-friendly refrigerant with a low global warming potential (GWP), low viscosity, and surface tension as well as high  $(dp/dT)_{sat}$ , so R1336mzz(Z) in the PHP experiences a low flow resistance during oscillation flow. Besides, the thermal stability and chemical inertness of R1336mzz(Z) enable it to have a long service life in high-temperature environments, which ensures the reliability and safety of the system. Bao et al. [36] have preliminarily demonstrated the use of R1336mzz(Z) as a working fluid for PHPs. Compared with water, specific heat capacity, thermal conductivity, and latent heat of vaporization of R1336mzz(Z) are significantly smaller, so the heat transfer capacity of R1336mzz(Z) is relatively weak at the same heat input. Therefore, R1336mzz(Z) was selected as a representative working fluid with good flow properties and relatively poor heat transfer capability. In addition, since the key thermal parameters of ethanol (except for the liquid viscosity, which is slightly larger than that of water) are in the range between water and R1336mzz(Z), ethanol was also chosen as a working fluid to examine the effect of the thermal properties of working fluid on the operation performance of PHPs at different heat transfer distances.

In addition, thermal resistance was an important index to evaluate the heat transfer performance of the PHP in the simulation, which was calculated by:

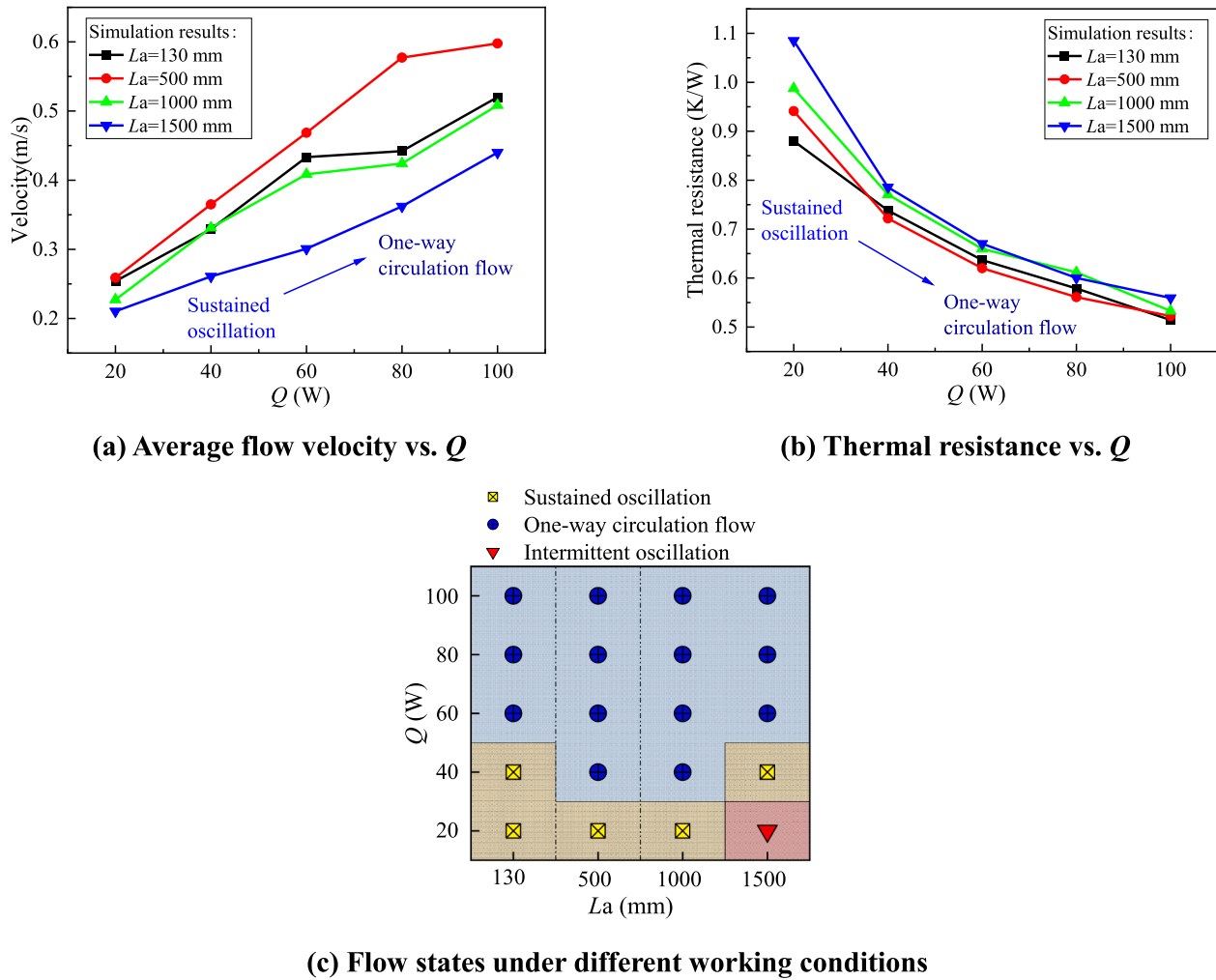


Fig. 20. Operating characteristics of R1336mzz(Z)-PHPs.

$$\overline{T}_c = \frac{\sum_{k=1}^{15} T_k}{15} \quad (46)$$

$$\overline{T}_e = \frac{\sum_{k=1}^{10} T_k}{10} \quad (47)$$

$$R = (\overline{T}_e - \overline{T}_c)/Q \quad (48)$$

Where  $\overline{T}_c$  (°C) was the average wall temperature of the condensation section and  $\overline{T}_e$  (°C) was the average wall temperature of the evaporation section. Fig. 7 showed the thermal resistance obtained from the simulation of the PHP with different unit sizes at the same operating condition ( $L_a=130$  mm and  $Q=20$  W). To ensure the accuracy of the model and improve computational efficiency, the unit size was chosen as 1 mm.

### 3. Partial visualization experiment of the PHP for validation

To verify the reliability of the theoretical model and test the working performance of PHPs under different heat transfer distances, partial visualization experiments of PHPs were conducted. The flow and heat transfer performance of PHPs was explored through experiments.

#### 3.1. Experimental setup

Fig. 8 showed the experimental setup for PHPs at different heat

transfer distances, which was similar to the setup described in the literature [38].

The experimental setup comprised four primary components: the pulsating heat pipe, the heating system, the cooling system, and the data collection system. The pulsating heat pipe was made of copper and glass tubes. The tubes provided a visual window in the adiabatic section. The dimensional parameters of the PHP used in the study were listed in Table 4. The lengths of the condensation and evaporation sections remained fixed during experiments, while the heat transfer distance can be adjusted by disassembling the joints in the adiabatic section and replacing them with capillary copper tubes of varying lengths. The visual window was designed to observe the flow characteristics of the working fluid at different heat transfer distances. The cooling system included a water pump, a cooling water tank, and a thermostatic bath. In this experiment, water was served as the coolant in the thermostatic bath, and the temperature was set to 20 °C. The thermostatic bath maintained a temperature fluctuation of  $\leq 0.01$  °C/30 min and temperature uniformity of  $\pm 0.01$  °C. The water pump circulated the 20 °C cooling water from the bath to the cooling tank at the condensation section, ensuring efficient cooling. The heating system consisted of a power meter, an adjustable DC-regulated power supply, and a nickel-chromium (Cr20Ni80) heating wire. The data collection system consists of an Agilent 34970A data logger, T-type thermocouples, and pressure transducers.

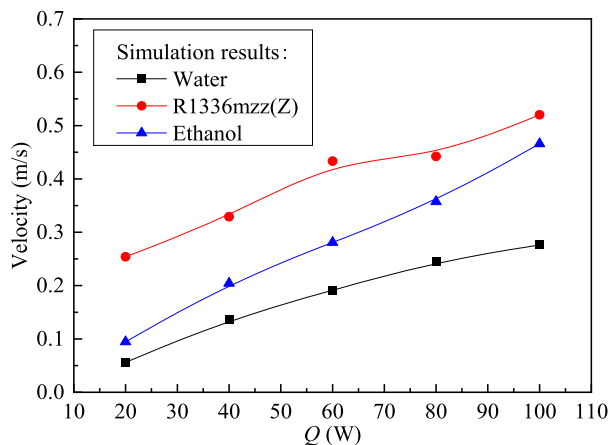
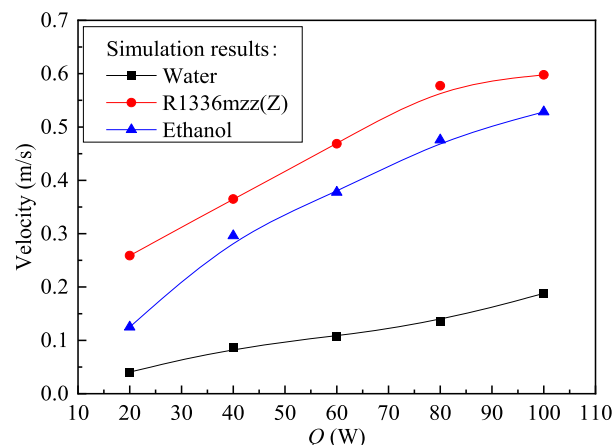
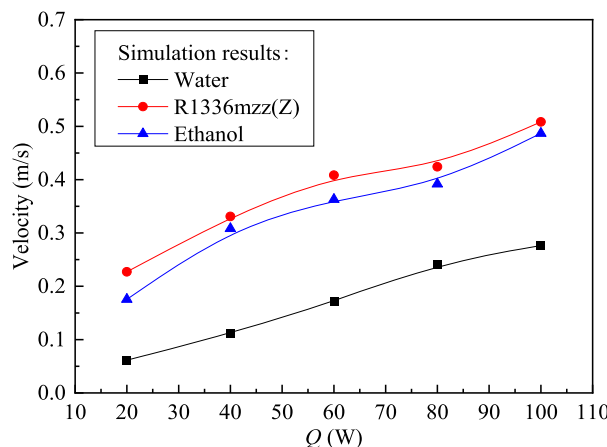
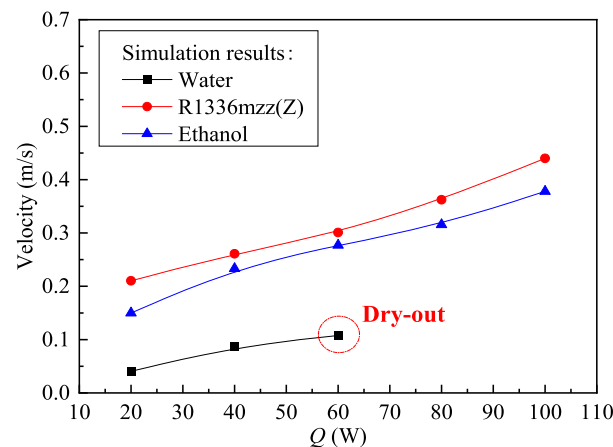
(a)  $La=130$  mm(b)  $La=500$  mm(c)  $La=1000$  mm(d)  $La=1500$  mm

Fig. 21. Variation of the average velocity of liquid slugs with heat input under different working fluids.

### 3.2. Experimental procedure and uncertainty analysis

Table 5 presented the experimental operation conditions. The PHP was pre-treated before the experiment started. During the pre-treatment stage, the PHP was cleaned with R1336mzz(z), and the internal wall was dried by blowing out the fluid with high-pressure nitrogen. A vacuum pump was then employed to evacuate the PHP until the internal pressure dropped below 2 Pa. The PHP was subsequently filled with the working fluid according to the specified filling ratio (FR = 0.5). The thermostat tank's water temperature was fixed at 20 °C. Once the temperature stabilized, the cooling water pump was activated to circulate water between the thermostat tank and the cooling water tank of the PHP at a flow rate of 3 L/min. During the experiments, the voltage and current outputs of the DC-regulated power supply were modified to vary the heat input in the evaporation section, ranging from 10 W to 100 W. A video camera was employed to capture the flow motion of the working fluid inside the PHP. The start-up time and temperature data were collected after the PHP had stabilized for approximately 10 min. After each set of experiments, the DC power supply was turned off, and the PHP was permitted to cool to room temperature prior to commencing the subsequent set of experiments.

The uncertainty of the instruments and measurement parameters used in the experiments was detailed in the literature [25]. According to the literature [25], the uncertainties of the temperature and heat input were calculated to be  $\pm 0.203$  °C and  $\pm 0.4$  W, respectively. The uncertainty of thermal resistance was derived by:

$$\delta R = \sqrt{\left(\frac{\partial R}{\partial T}\right)(\delta T)^2 + \left(\frac{\partial R}{\partial Q}\right)(\delta Q)^2} \quad (49)$$

The maximum relative uncertainty of thermal resistance was calculated to be 8.03 %.

## 4. Results and discussion

### 4.1. Validation of the theoretical model

#### 4.1.1. Comparison of simulation and experimental results

Fig. 9 showed the flow states of R1336mzz(Z) observed during the experiment, and Fig. 10 summarized and compared the theoretical and experimental flow states under different operating conditions. From Fig. 9, the visualized experimental results aligned with theoretical predictions. As heat input increased across various heat transfer distances, R1336mzz(Z) transitioned from oscillatory flow to unidirectional flow, confirming the reliability of the theoretical model.

Fig. 11 compared the transient temperatures at measurement point 1 obtained from experiments and simulation during steady-state operation. As shown in Fig. 11(a), when the heat transfer distance was 1500 mm and heat input was 20 W, the working fluid oscillated intermittently and the temperature fluctuation amplitudes at measurement point 1 obtained experimentally and theoretically were approximate. As shown in Fig. 11(b)-(c), when there was no sudden temperature rise caused by

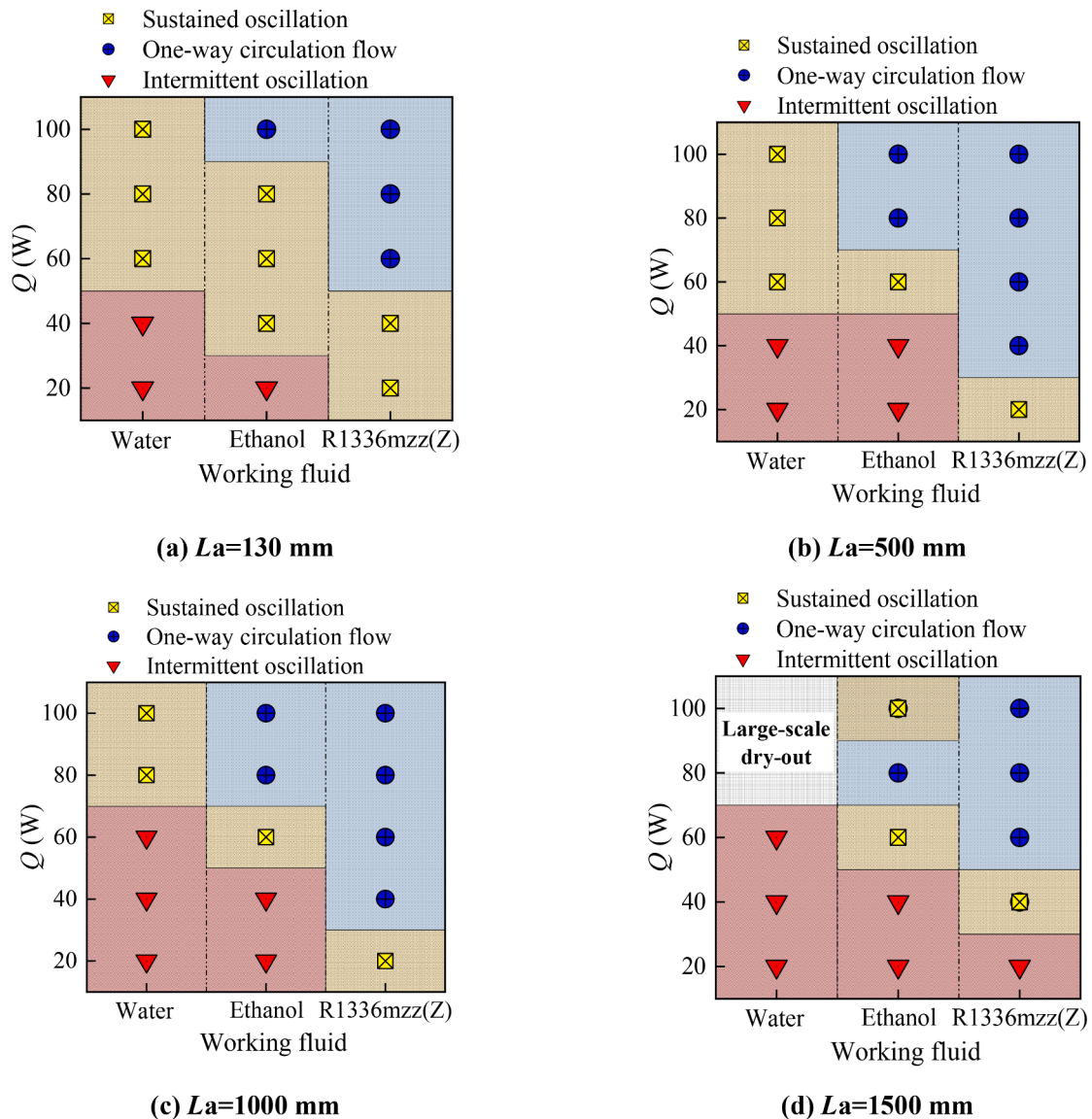


Fig. 22. Flow states at different heat transfer distances during simulation.

local dry-out, the temperature differences between experimental and simulation results were mostly within  $\pm 5^\circ\text{C}$ .

Fig. 12 displayed the variation of  $R_{\text{exp}}$  with heat input, and Fig. 13 summarized and compared the experimental and theoretical thermal resistance values. From Figs. 12 and 13, it can be observed that at low heat input, the thermal resistance of the R1336mzz(Z)-PHP increased gradually with heat transfer distances. However, at high heat input, thermal resistance remained similar across different heat transfer distances. This was primarily because, at low heat input, the overall flow velocity was low, causing a poor heat transfer capability. As the heat input increased, the pressure difference rose, leading to a greater driving force. This promoted unidirectional flow in the R1336mzz(Z)-PHP. What's more, the deviation between the thermal resistance values from experimental results and numerical simulations was generally within  $\pm 10\%$ , demonstrating good agreement and confirming the accuracy of the numerical simulations.

#### 4.1.2. Comparison of simulation results with those in the literatures

To further validate the accuracy of the theoretical model, the numerical simulation results were systematically compared with both similarly structured simulations and experimental data available in the literature. Table 6 listed the operating parameters of the experimental/

theoretical cases used for validation. Fig. 14 presented a comparison of the thermal resistance obtained from the simulations in the present study with those of the previous study. According to Fig. 14, the thermal resistance of PHP in other theoretical studies [9,16] decreased with the increase of heat input, and this trend was consistent with the results of the present study. In addition, the simulation results in the present study were close to the experimental results of Liu et al. [38]. This consistency highlights the reliability and accuracy of the theoretical model developed in this study.

#### 4.2. Flow and heat transfer characteristics of PHPs

Figs. 15–17 illustrated the variation of flow states, temperature, and pressure with time in PHPs during operation, respectively. According to Figs. 15–17, it can be observed that dynamic processes such as the formation and merging of liquid slugs, and the generation and expansion of vapor plugs occurred during operation. Besides, the flow motion was strongly associated with the changes in temperature and pressure. As the evaporation temperature rose, the pressure difference between the evaporation and condensation sections gradually increased, providing a stronger driving force. The stronger driving force pushed the vapor plugs in the evaporation section to move toward the condensation section. The

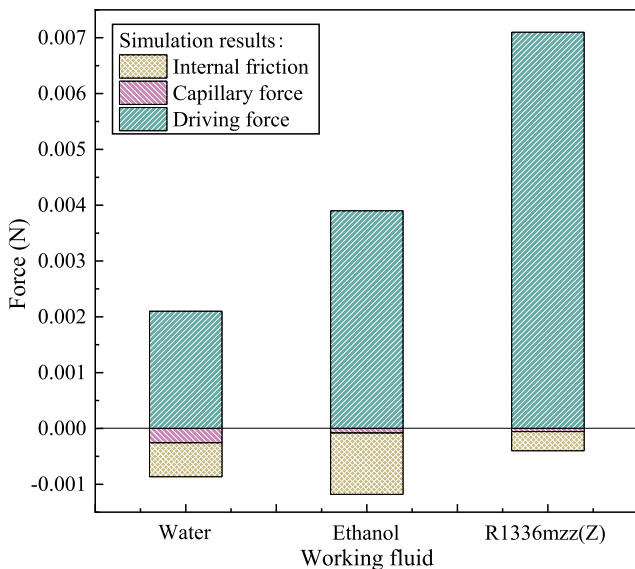


**Fig. 23.** Force analysis of liquid slug at measurement point 10 ( $La=130$  mm,  $Q=20$  W,  $t=23.4$  s).

liquid from the condensation section returned to the evaporation section under the influence of gravity, replenishing the liquid consumed by phase change. The liquid replenishment lowered the evaporation temperature in turn.

**Fig. 18** illustrated the variation of momentum of all liquid slugs with time and **Fig. 19** displayed the temperature fluctuation under three typical flow states. As indicated in **Figs. 18 and 19**, during the operation, the working fluid exhibited three typical flow states: intermittent oscillation, continuous oscillation, and unidirectional flow. When the working fluid exhibited intermittent oscillation, stagnancy (zero momentum) and flow reactivation (a sharp increase in momentum) occurred alternately. When the working fluid stagnated, the evaporation temperature climbed quickly, and the pressure difference widened dramatically. Once the pressure difference reached a certain threshold, the working fluid would be driven to start oscillating again, causing the evaporation temperature to gradually decrease. Consequently, stagnation caused pronounced temperature fluctuations in the evaporation section. In contrast, when the working fluid exhibited continuous oscillation or unidirectional flow, PHPs achieved more stable and efficient heat transfer, representing the ideal operating condition. Besides, it's worth noting that when the working fluid stagnated, the liquid film in the evaporation section gradually became thinner, and the liquid film in some regions might be even lower than the critical value, which made the phenomenon of local dry-out occur. At this time, the temperature rise rate in this region was significantly higher than that in other regions, as shown in **Fig. 19(a)**. In addition, unlike large-scale dry-out [25], local

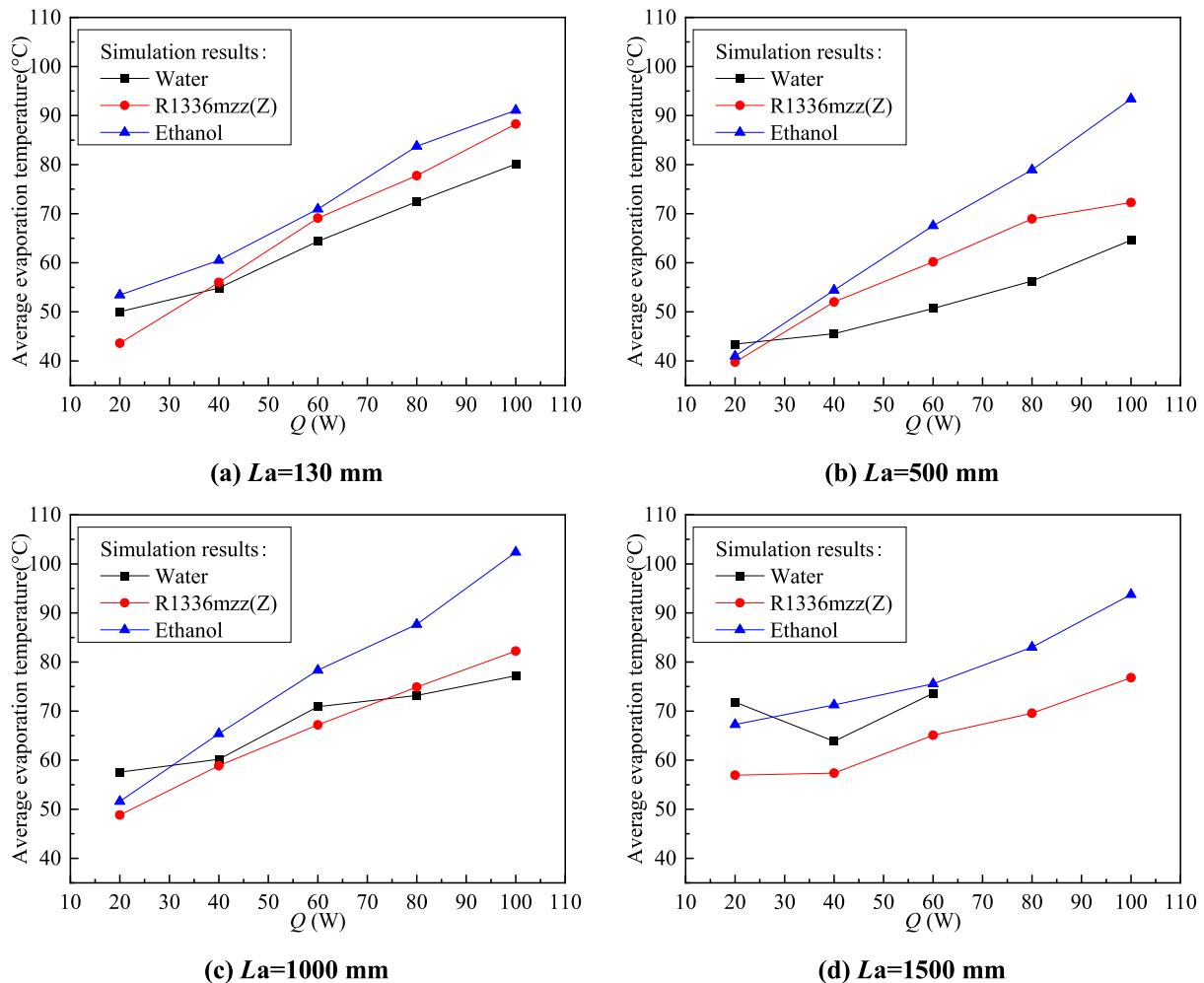


**Fig. 24.** Variation of evaporation temperature with heat input for PHPs filled with various working fluids.

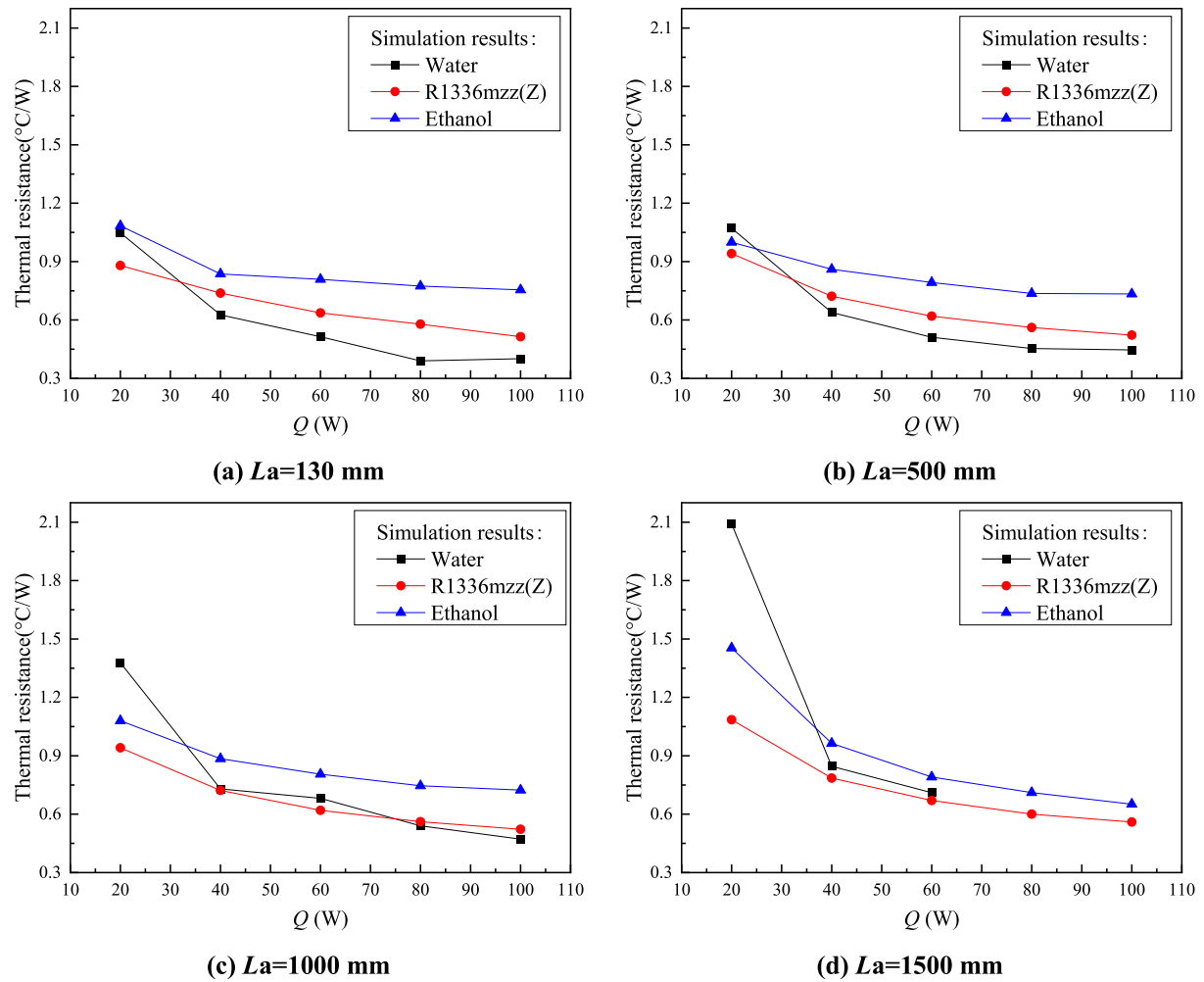


**Fig. 25.** Variation of thermal resistance with heat input for PHPs filled with various working fluids.

dry-out was recoverable, but it significantly exacerbated the evaporation temperature fluctuation.

#### 4.3. Effect of heat transfer distance on the flow and heat transfer characteristics

Fig. 20 showed the operating characteristics (average flow velocity, thermal resistance and flow states) of the R1336mzz(Z)-PHPs with different heat transfer distances during steady-state operation. The average flow velocity was calculated by:

$$\bar{v} = \frac{\sum_{i=1}^{10} |v_i|}{10} \quad (50)$$

Where  $|v_k|$  was the absolute value of the velocity of the working fluid at measurement point  $k$ , and  $\bar{|v_k|}$  was the time-averaged value of  $|v_k|$  during the steady-state operation of the PHP. As seen in Fig. 20, as the heat input grew, the velocity of the liquid slug gradually rose, while thermal resistance decreased. The flow state of the working fluid shifted from continuous oscillation to unidirectional flow. When the heat input reached or exceeded 60 W, the working fluid inside R1336mzz(Z)-PHPs with different heat transfer distances all achieved unidirectional circulation flow. The flow and heat transfer performance of the PHP tended to first increase and then decrease with heat transfer distance, suggesting that there is an optimal heat transfer distance that maximizes the performance of the PHP. The optimal heat transfer distance of the PHP

simulated was within the range of 130 mm to 1000 mm. The main reason was that an appropriate increase in the heat transfer distance provided enough space and time for the working fluid in the PHP to develop a regular and stable flow, thus enhancing the flow performance of the working fluid. A better flow performance was conducive to the sensible and latent heat transfer between the evaporation section and condensation section. When the heat transfer distance was too long, the distribution of liquid slugs and vapor plugs in the PHP became more uneven. Liquid plugs accumulated in some areas, which increased the flow resistance. When the flow resistance was too big for the working fluid to form sustained oscillation, the working fluid stagnated, inducing the local dry-out in the PHP. The local dry-out exacerbated the temperature fluctuations in the evaporation section, thereby reducing the heat transfer ability of the PHP.

#### 4.4. Comparison of flow and heat transfer performance of PHPs with various working fluids

To scientifically justify the selection of the working fluids and comprehensively evaluate their impact on the operating performance of PHPs, water, ethanol and R1336mzz(Z) were selected as three typical working fluids of PHPs in this study. The flow and heat transfer characteristics of PHPs with different working fluids were compared and the advantages of R1336mzz(Z) as a working fluid of PHPs were further explored.

Fig. 21 showed the variation of the average velocity of liquid slugs

with heat input in PHPs filled with various working fluids and Fig. 22 illustrated the flow states of various working fluids at different heat transfer distances. As seen in Figs. 21 and 22, the average velocity of the working fluid in the R1336mzz(Z)-PHP was significantly higher. R1336mzz(Z) succeeded in transitioning from oscillatory flow to unidirectional flow at various heat transfer distances, while water-PHPs exhibited large-scale dry-out phenomena at long heat transfer distances. The average values of driving force, capillary force, and internal friction acting on the liquid slug during steady-state operation were compared in Fig. 23. According to Fig. 23, the driving force exerted on the liquid slug was highest for R1336mzz(Z), followed by ethanol, and lowest for water. In contrast, capillary resistance was highest for water, followed by ethanol, and lowest for R1336mzz(Z). The results indicated that R1336mzz(Z) had the strongest flow characteristics across different heat transfer distances, followed by ethanol, with water showing the weakest flow performance. This was mainly due to the fact that R1336mzz(Z) had a higher  $(dp/dT)_{sat}$ , a smaller latent heat of vaporization and a lower viscosity compared to water and ethanol. The smaller latent heat of vaporization results in a faster phase change rate of the working fluid at the same heat input, and the higher  $(dp/dT)_{sat}$  led to a larger pressure difference at the same temperature difference. These contributed to a larger driving force to accelerate the flow velocity of the working fluid. Besides, due to the lower viscosity, R1336mzz(Z) experienced less internal friction. Therefore, R1336mzz(Z) achieved the best flow performance at the same heat input.

In addition, according to Fig. 22, the severe local dry-out phenomenon occurred mostly at low heat input. When the heat input was high, the working fluid in the PHP formed a continuous oscillation or unidirectional circulation flow, which effectively avoided the occurrence of local dry-out. This was mainly because when the heat input was low, the driving force was not big enough to maintain the sustained flow of the working fluid. Flow stagnation led to the untimely liquid replenishment of the dry area, inducing the appearance of local dry-out. When the heat input was high, the working fluid had sufficient driving force to form a stable flow. What's more, local dry-out was also closely related to the thermal properties of the working fluid. The working fluid with a low viscosity, a small latent heat of vaporization and a high  $(dp/dT)_{sat}$ , had a better anti-dry-out ability. The main reason was that the small viscosity, small latent heat of vaporization and high  $(dp/dT)_{sat}$  helped to develop a large driving force and small flow resistance, allowing the liquid film to be replenished quickly. The sufficient liquid replenishment effectively suppressed the local dry-out.

Figs. 24 and 25 showed the variation of average evaporation temperature and thermal resistance with heat input for PHPs filled with different working fluids. According to Fig. 25, the thermal resistance of the R1336mzz(Z)-PHP was relatively the lowest when the heat transfer distance was small (130 mm and 500 mm) and the heat input was 20 W. This was because the heat transfer capability of PHPs was greatly influenced by the flow properties of the working fluids at a comparatively low heat input. The oscillation frequency of water was low at 20 W, so the stagnation time was long. A long stagnation time resulted in large temperature fluctuations in the evaporation section and might cause severe local dry-out. When the heat input increased to 40 W, water in the PHP no longer had a long stagnation time, and its heat transfer performance was greatly improved. The heat transfer coefficient in the water-PHP was larger than that of ethanol and R1336mzz(Z) due to the higher thermal conductivity and specific heat capacity of water. Therefore, the thermal resistance of the water-PHP was significantly smaller than that of the R1336mzz(Z)-PHP and ethanol-PHP at high heat input when the heat transfer distance was small (130 mm and 500 mm). When the heat transfer distance was large (1000 mm and 1500 mm), the R1336mzz(Z)-PHP had a superior heat transfer capability compared to the water-PHP and ethanol-PHP. The main reason was that the path of the liquid slugs back from the cold end to the hot end increased when the heat transfer distance was larger, making the liquid replenishment in the evaporation section more difficult. The liquid replenishment was an

essential factor impact on the heat transfer capability of the PHP, so the heat transfer performance at a larger heat transfer distance was relatively more affected by the velocity of the working fluid. Since the flow velocity inside the R1336mzz(Z)-PHP was significantly higher compared to the ethanol-PHP and water-PHP, the R1336mzz(Z)-PHP showed a relatively better heat transfer performance at a large heat transfer distance. In addition, the thermal resistance of PHPs with various working fluids at 20 W increased with the growth of the heat transfer distance. At 20 W, the thermal resistances of the water-PHP, ethanol-PHP, and R1336mzz(Z)-PHP increased by 99.6 %, 34.1 %, and 23.3 %, respectively, when the heat transfer distance was enlarged from 130 mm to 1500 mm. This indicated that the deterioration of the heat transfer performance of water-PHPs was the highest at low heat input with the increase of heat transfer distance, while the heat transfer performance of R1336mzz(Z)-PHPs was relatively least affected by the heat transfer distance.

In summary, R1336mzz(Z)-PHPs maintained relatively good flow and heat transfer performance at various heat transfer distances and didn't deteriorate significantly as the heat transfer distance was extended. Therefore, R1336mzz(Z)-PHPs had great potential for applications over long heat transfer distances.

## 5. Conclusions

In this work, a two-phase heat and mass transfer model incorporating liquid film dynamics was established and partial visualization experiments were conducted to validate the reliability of the theoretical model. Based on these, the flow and heat transfer performance of PHPs under various heat transfer distances were numerically simulated and experimentally investigated. The flow and heat transfer characteristics of R1336mzz(Z)-PHPs were compared with water-PHPs and ethanol-PHPs to investigate the influence of working fluids on the operating performance of PHPs. The primary conclusions were as follows:

- (1) The two-phase heat and mass transfer model, incorporating liquid film dynamics, was developed to capture the local dry-out phenomenon and accurately simulate the heat and mass transfer process in PHPs. The model was validated experimentally, with experimental results closely aligning with numerical simulations. The deviation in thermal resistance between experimental and theoretical values was generally within  $\pm 10\%$ , confirming the accuracy and reliability of the theoretical model.
- (2) For R1336mzz(Z)-PHPs with varying heat transfer distances, both flow and heat transfer performance improved gradually as heat input rose. The impact of heat transfer distance was more pronounced at lower heat input. The flow and heat transfer performance tended to strengthen and then weaken with the increase of heat transfer distance, indicating an optimal heat transfer distance for peak performance.
- (3) Compared to water and ethanol, R1336mzz(Z) generated a greater driving force while experiencing lower flow resistance, resulting in a higher average flow velocity of the working fluid. This enabled the transition from oscillatory flow to one-way circulation flow at various heat transfer distances and avoided the occurrence of local dry-out, leading to superior flow performance.
- (4) Compared to water-PHPs and ethanol-PHPs, the performance of the R1336mzz(Z)-PHP was relatively less affected by heat transfer distance. Even at a large heat transfer distance, R1336mzz(Z) maintained superior flow and heat transfer performance.

## Funding

This work has been supported by the National Natural Science Foundation of China (No. 52076185) and the Natural Science

Foundation of Zhejiang Province (No. LZ19E060001).

## CRediT authorship contribution statement

**Ying Liu:** Writing – original draft, Investigation. **Yuhao Yan:** Investigation. **Xilei Wu:** Investigation. **Kangli Bao:** Investigation. **Jiali Yang:** Investigation. **Maojin Zeng:** Investigation. **Xiaohong Han:** Writing – review & editing, Funding acquisition.

## Declaration of competing interest

The authors declare that they have no known competing financial interests or personal relationships that could have appeared to influence the work reported in this paper.

## Acknowledgements

No additional individuals or organizations need to be acknowledged in this study.

## Data availability

Data will be made available on request.

## References

- [1] S. Naffziger, Future of AI hardware enabled by advanced packaging. (2024). [https://eps.ieee.org/images/files/HIR\\_Presentations/2.2Naffziger\\_ECTC\\_panel\\_presentation\\_0524.pdf](https://eps.ieee.org/images/files/HIR_Presentations/2.2Naffziger_ECTC_panel_presentation_0524.pdf).
- [2] Z. He, Y. Yan, Z. Zhang, Thermal management and temperature uniformity enhancement of electronic devices by micro heat sinks: a review, *Energy* 216 (2021) 119223, <https://doi.org/10.1016/j.energy.2020.119223>.
- [3] D. Zhang, L. Wang, B. Xu, Q. Li, S. Wang, Z. An, Experimental and simulation study on flow heat transfer characteristics of flat pulsating heat pipe with wide and narrow interphase channels, *Appl. Therm. Eng.* 245 (2024) 122806, <https://doi.org/10.1016/j.applthermaleng.2024.122806>.
- [4] X. Han, X. Wang, H. Zheng, X. Xu, G. Chen, Review of the development of pulsating heat pipe for heat dissipation, *Renew. Sustain. Energy Rev.* 59 (2016) 692–709, <https://doi.org/10.1016/j.rser.2015.12.350>.
- [5] V.S. Nikolayev, Physical principles and state-of-the-art of modeling of the pulsating heat pipe: a review, *Appl. Therm. Eng.* 195 (2021) 117111, <https://doi.org/10.1016/j.applthermaleng.2021.117111>.
- [6] F.K. Kholi, S. Park, J.S. Yang, M.Y. Ha, J.K. Min, A detailed review of pulsating heat pipe correlations and recent advances using Artificial Neural Network for improved performance prediction, *Int. J. Heat Mass Transf.* 207 (2023) 124010, <https://doi.org/10.1016/j.ijheatmasstransfer.2023.124010>.
- [7] S. Hong, J. Yu, C. Dang, A spring-mass-damper model based on separated phase flow mode for pulsating heat pipe with adjustable-structured channels, *Appl. Therm. Eng.* 257 (2024) 124275, <https://doi.org/10.1016/j.applthermaleng.2024.124275>.
- [8] M. Opalski, C. Czajkowski, P. Blasiak, A.I. Nowak, J. Ishimoto, S. Pietrowicz, Comprehensive numerical modeling analysis and experimental validation of a multi-turn pulsating heat pipe, *Int. Commun. Heat Mass Transf.* 159 (2024) 107990, <https://doi.org/10.1016/j.icheatmasstransfer.2024.107990>.
- [9] J. Bae, S.Y. Lee, S.J. Kim, Numerical investigation of effect of film dynamics on fluid motion and thermal performance in pulsating heat pipes, *Energy Conv. Manag.* 151 (2017) 296–310, <https://doi.org/10.1016/j.enconman.2017.08.086>.
- [10] G. Spinato, N. Borhani, J.R. Thome, Operational regimes in a closed loop pulsating heat pipe, *Int. J. Therm. Sci.* 102 (2016) 78–88, <https://doi.org/10.1016/j.ijthermalsci.2015.11.006>.
- [11] M. Rao, F. Lefèvre, S. Khandekar, J. Bonjour, Heat and mass transfer mechanisms of a self-sustained thermally driven oscillating liquid-vapour meniscus, *Int. J. Heat Mass Transf.* 86 (2015) 519–530, <https://doi.org/10.1016/j.ijheatmasstransfer.2015.03.015>.
- [12] I. Nebrashevych, V.S. Nikolayev, Effect of tube heat conduction on the pulsating heat pipe start-up, *Appl. Therm. Eng.* 117 (2017) 24–29, <https://doi.org/10.1016/j.applthermaleng.2017.02.013>.
- [13] M.B. Shafii, A. Faghri, Y. Zhang, Thermal modeling of unlooped and looped pulsating heat pipes, *J. Heat Transfer J. Heat Transfer* 123 (2001) 1159–1172, <https://doi.org/10.1115/1.1409266>.
- [14] K. Bao, Y. Zhuang, X. Gao, Y. Xu, X. Wu, X. Han, Transient numerical model on the design optimization of the adiabatic section length for the pulsating heat pipe, *Applied Sciences* 11 (2021), <https://doi.org/10.3390/app11209432>.
- [15] X. Sun, S. Li, B. Wang, B. Jiao, J. Pfotenhauer, F. Miller, Z. Gan, Numerical study of the thermal performance of a hydrogen pulsating heat pipe, *Int. J. Therm. Sci.* 172 (2022) 107302, <https://doi.org/10.1016/j.ijthermalsci.2021.107302>.
- [16] M. Mameli, M. Marengo, S. Zinna, Numerical model of a multi-turn closed loop pulsating heat pipe: effects of the local pressure losses due to meanderings, *Int. J. Heat Mass Transf.* 55 (2012) 1036–1047, <https://doi.org/10.1016/j.ijheatmasstransfer.2011.10.006>.
- [17] H.Y. Noh, S.J. Kim, Numerical simulation of pulsating heat pipes: parametric investigation and thermal optimization, *Energy Conv. Manag.* 203 (2020) 112237, <https://doi.org/10.1016/j.enconman.2019.112237>.
- [18] M. Manzoni, M. Mameli, C. de Falco, L. Araneo, S. Filippeschi, M. Marengo, Non equilibrium lumped parameter model for pulsating heat pipes: validation in normal and hyper-gravity conditions, *Int. J. Heat Mass Transf.* 97 (2016) 473–485, <https://doi.org/10.1016/j.ijheatmasstransfer.2016.02.026>.
- [19] T. Daimaru, S. Yoshida, H. Nagai, Study on thermal cycle in oscillating heat pipes by numerical analysis, *Appl. Therm. Eng.* 113 (2017) 1219–1227, <https://doi.org/10.1016/j.applthermaleng.2016.11.114>.
- [20] I. Nebrashevych, V.S. Nikolayev, Pulsating heat pipe simulations: impact of PHP Orientation, *Microgravity Sci. Technol.* 31 (2019) 241–248, <https://doi.org/10.1007/s12217-019-9684-3>.
- [21] P. Sakulchangsatjai, P. Chareonsawan, T. Waowae, P. Terdtoon, M. Murakami, Mathematical modeling of closed-end pulsating heat pipes operating with a bottom heat mode, *Heat Transf. Eng.* 29 (2008) 239–254, <https://doi.org/10.1080/01457630701756173>.
- [22] C. Czajkowski, A.I. Nowak, P. Blasiak, A. Ochman, S. Pietrowicz, Experimental study on a large scale pulsating heat pipe operating at high heat loads, different adiabatic lengths and various filling ratios of acetone, ethanol, and water, *Appl. Therm. Eng.* 165 (2020) 114534, <https://doi.org/10.1016/j.applthermaleng.2019.114534>.
- [23] M. Arab, M. Soltanieh, M.B. Shafii, Experimental investigation of extra-long pulsating heat pipe application in solar water heaters, *Exp. Therm. Fluid Sci.* 42 (2012) 6–15, <https://doi.org/10.1016/j.expthermflusci.2012.03.006>.
- [24] Y. Shi, J. Yan, Y. Zhou, D. Xu, L. Li, Experimental study on nitrogen pulsating heat pipes with different heat transmission distances and configurations, *Cryogenics (Guildf)* 141 (2024) 103898, <https://doi.org/10.1016/j.cryogenics.2024.103898>.
- [25] Y. Liu, K. Bao, Y. Yan, H. Ouyang, X. Han, Investigation on the influence of different heat transmission distances on thermo-hydrodynamic characteristics of pulsating heat pipes, *Appl. Therm. Eng.* 234 (2023) 121284, <https://doi.org/10.1016/j.applthermaleng.2023.121284>.
- [26] S.W. Churchill, M. Bernstein, A correlating equation for forced convection from gases and liquids to a circular cylinder in crossflow, *J. Heat Transfer* 99 (1977) 300–306, <https://doi.org/10.1115/1.3450685>.
- [27] E.J. Davis, G.H. Anderson, The incipience of nucleate boiling in forced convection flow, *AICHE J.* 12 (1966) 774–780, <https://doi.org/10.1002/aic.690120426>.
- [28] R.H.S. Winterton, Where did the Dittus and Boelter equation come from? *Int. J. Heat Mass Transf.* 41 (1998) 809–810, [https://doi.org/10.1016/S0017-9310\(97\)00177-4](https://doi.org/10.1016/S0017-9310(97)00177-4).
- [29] V. Gnielinski, New equations for heat and mass transfer in the turbulent flow in pipes and channels, *NASA STI/Recon. Techn. Report A* 41 (1975) 8–16.
- [30] I.L. Piioro, Experimental evaluation of constants for the Rohsenow pool boiling correlation, *Int. J. Heat Mass Transf.* 42 (1999) 2003–2013, [https://doi.org/10.1016/S0017-9310\(98\)00294-4](https://doi.org/10.1016/S0017-9310(98)00294-4).
- [31] G. Su, F. Paolo D'Aleo, B. Phillips, E. Al-Safran, J. Buongiorno, H. Prasser, Suppression of nucleate boiling in upward two-phase annular flow: a direct measurement using modern diagnostics, *Int. J. Heat Mass Transf.* 159 (2020) 120143, <https://doi.org/10.1016/j.ijheatmasstransfer.2020.120143>.
- [32] H. Zhao, Engineering Fluid Mechanics, 1 ed.: Huazhong University of Science and Technology (HUST) Press.
- [33] J. Qu, Q. Wang, C. Li, X. Han, Z. He, A simple model for Taylor flow induced contact angle hysteresis and capillary pressure inside mini/micro-scale capillary tubes, *Int. J. Heat Mass Transf.* 78 (2014) 1004–1007, <https://doi.org/10.1016/j.ijheatmasstransfer.2014.07.048>.
- [34] J.R. Thome, V. Dupont, A.M. Jacobi, Heat transfer model for evaporation in microchannels. Part I: presentation of the model, *Int. J. Heat Mass Transf.* 47 (2004) 3375–3385, <https://doi.org/10.1016/j.ijheatmasstransfer.2004.01.006>.
- [35] Y. Han, N. Shikazono, The effect of bubble acceleration on the liquid film thickness in micro tubes, *Int. J. Heat Fluid Flow*. 31 (2010) 630–639, <https://doi.org/10.1016/j.ijheatfluidflow.2010.02.002>.
- [36] K. Bao, Y. Liu, Y. Yan, G. Ye, X. Han, Partial visualization study on flow, startup and heat transfer characteristics of closed-loop pulsating heat pipe with R1336mzz (Z), *Appl. Therm. Eng.* 226 (2023) 120218, <https://doi.org/10.1016/j.applthermaleng.2023.120218>.
- [37] L.E. W., B.I. H., H.M. L., NIST Standard Reference Database 23: Reference Fluid Thermodynamic and Transport properties-REFPROP, 10.0 ed., NIST, 2018.
- [38] Y. Liu, Y. Yan, K. Bao, X. Wu, J. Yang, N. Jiang, X. Han, Effect of localized dry-out on startup and steady-state operation characteristics of ethanol-based oscillating heat pipes, *Appl. Therm. Eng.* 257 (2024) 124420, <https://doi.org/10.1016/j.applthermaleng.2024.124420>.